A Raman spectroscopic study of organic matter in interplanetary dust particles and meteorites using multiple wavelength laser excitation

Journal Item

The Meteoritical Society

Meteoritics & Planetary Science 48, Nr 10, 1800–1822 (2013)
doi: 10.1111/maps.12196

A Raman spectroscopic study of organic matter in interplanetary dust particles and meteorites using multiple wavelength laser excitation

N. A. STARKEY[1*], I. A. FRANCHI[1], and C. M. O'D. ALEXANDER[2]

[1]Planetary and Space Sciences, The Open University, Walton Hall, Milton Keynes MK7 6AA, UK
[2]Department of Terrestrial Magnetism, Carnegie Institution of Washington, 5241 Broad Branch Road, NW, Washington, District of Columbia 20015–1305, USA
[*]Corresponding author. E-mail: natalie.starkey@open.ac.uk

(Received 04 February 2013; revision accepted 30 July 2013)

Abstract–Raman spectroscopy was used to investigate insoluble organic matter (IOM) from a range of chondritic meteorites, and a suite of interplanetary dust particles (IDPs). Three monochromatic excitation wavelengths (473 nm, 514 nm, 632 nm) were applied sequentially to assess variations in meteorite and IDP Raman peak parameters (carbon D and G bands) as a function of excitation wavelength (i.e., dispersion). Greatest dispersion occurs in CVs > OCs > CMs > CRs with type 3 chondrites compared at different excitation wavelengths displaying conformable relationships, in contrast to type 2 chondrites. These findings indicate homogeneity in the structural nature of type 3 chondrite IOM, while organic matter (OM) in type 2 chondrites appears to be inherently more heterogeneous. If type 2 and type 3 chondrite IOM shares a common source, then thermal metamorphism may have a homogenizing effect on the originally more heterogeneous OM. IDP Raman G bands fall on an extension of the trend displayed by chondrite IOM, with all IDPs having Raman parameters indicative of very disordered carbon, with almost no overlap with IOM. The dispersion effect displayed by IDPs is most similar to CMs for the G band, but intermediate between CMs and CRs for the D band. The existence of some overlapping Raman features in the IDPs and IOM indicates that their OM may share a common origin, but the IDPs preserve more pristine OM that may have been further disordered by ion irradiation. H, C, and N isotopic data for the IDPs reveal that the disordered carbon in IDPs corresponds with higher $\delta^{15}N$ and lower $\delta^{13}C$.

INTRODUCTION

Raman spectroscopy, hereafter termed Raman, can be used to investigate the nature of organic matter present in bulk meteorites, in insoluble organic matter (IOM) extracted by demineralization of bulk meteorites, and in interplanetary dust particles (IDPs). When applied at low laser power, Raman is a nondestructive technique that can yield information on the structural order of polyaromatic organic matter. The structural order of the carbon is represented by the Raman spectra of the first-order band peaks at approximately 1582 cm^{-1} for the G band and 1350 cm^{-1} for the D band (Tuinstra and Koenig 1970), and the second-order D′ band at approximately 1620 cm^{-1} and the G′ band at 2700 cm^{-1}. The measured Raman bands do not represent absolute wave numbers, but instead represent frequencies shifted relative to the wavelength used to excite Raman scattering. The G band is Raman-active for sp^2 (an electronic configuration of carbon) carbon networks, representing the inplane stretching mode of all pairs of sp^2 atoms in rings. As such, the G band can be used to distinguish between different types of carbon materials (Ferrari and Robertson 2001) and is present in organic matter regardless of the degree of structural order. The D band is due to structural defects, originating from the breathing motion of sp^2 atoms in rings (Tuinstra and Koenig 1970; Ferrari and Robertson 2001), and would not be present in perfectly stacked graphite. The dispersive nature of the D band (where dispersion is defined as the shift in the measured band frequency as a function of

excitation wavelength) was first reported by Vidano et al. (1981). They tested a wide range of sp^2 carbon materials and showed that the dispersion of the D band is linear, with its frequency upshifting with increasing excitation energy. It was also noted that the slope of the dispersion (i.e., the change in band frequency with the change in excitation energy) was independent of the type of carbon material being investigated. In principle, the first-order G band is totally independent of the wavelength used to excite Raman scattering so that it should not show any dispersion. However, it can appear that the G band exhibits dispersion because the D′ band that sits, unresolved, at a slightly higher frequency than the first-order G band and, in most circumstances, overlaps with it, is defect-induced and does show dispersion (Matthews et al. 1999). In practice, this results in the G band (which can therefore be viewed as a type of "hybrid" band) itself appearing to show dispersion when, in fact, it is only the D′ that is affected. In this study, we investigate the Raman features of a range of meteoritic IOM and IDPs by sequentially applying three individual excitation wavelengths. The framework provided by earlier, and ongoing, studies into more simple carbon materials allows us to investigate the more complex carbon present in these natural meteoritic samples to understand more about their conditions of formation.

Most of the carbon in primitive chondritic meteorites is present as organic material, which can be broadly divided into solvent-soluble and -insoluble components (Gilmour 2003). The soluble material is composed of a complex mix of species, including a wide range of carboxylic acids, amino acids, and many other compounds. The much more abundant IOM, on the other hand, is macromolecular and composed of small polycyclic aromatic hydrocarbons (PAH) whose hydrogen atoms are highly substituted by short, highly branched aliphatic chains, ethers, and furans (Hayatsu et al. 1977; Alexander et al. 1998; Cody et al. 2002, 2011; Remusat et al. 2005; Sephton et al. 2005). How the organic components formed is not well understood, and adding to the confusion is the considerable chemical and isotopic inter- and intragroup heterogeneity of the organic matter in chondrites, including the IOM, which is the focus of this paper.

The IOM present in chondrites will have undergone complex histories involving processes that occurred both before and after incorporation into the various chondrite parent bodies (Gilmour 2003). While there are many proposed formation theories to explain the chemical and isotopic heterogeneity of IOM in chondrites, these can mostly be grouped into two schools of thought. One school assumes that all chondrites accreted the same precursor organic matter from the solar nebula, and that differences observed in the IOM between different chondrites are the result of thermal and/or aqueous processing that occurred in the meteorite parent bodies (Alexander et al. 1998, 2010; Quirico et al. 2003; Cody and Alexander 2005; Cody et al. 2011). The other school regards parent-body alteration as being unable to account for IOM heterogeneity, and instead suggests that it reflects heterogeneities inherited directly from the protosolar nebula (Yang and Epstein 1983; Messenger 2000; Busemann et al. 2006; Remusat et al. 2009, 2010; Robert et al. 2011). In general, the chondrites are classified according to the extent of thermal or aqueous alteration that is recorded in their silicate mineralogy. However, in some cases, systematic changes in Raman peak parameters of IOM among chondrites from a particular group (e.g., CO and CV chondrites) have been used to provide an independent scale of metamorphism (Quirico et al. 2003; Bonal et al. 2006a, 2007; Busemann et al. 2007). For instance, Busemann et al. (2007) demonstrated that there are systematic trends in Raman parameters that correlate with meteorite classification and IOM chemical composition. They also showed that trends for thermal metamorphism, terrestrial weathering, and amorphization due to irradiation in space could be identified, demonstrating the practicality of Raman as a means for investigating chondrites.

Fine-grained anhydrous cometary IDPs have silicate mineralogies and textures that are very similar to those expected for primary condensates in the protoplanetary disk. Fraundorf et al. (1982) first reported the presence of carbon in IDPs by Raman measurements, and this work was followed up with more in-depth Raman studies characterizing IDPs (Wopenka 1988; Quirico et al. 2005). It has also been shown that the organic matter in chondritic-porous IDPs displays anomalous H, C, and N isotopic signatures (McKeegan et al. 1985; Messenger et al. 1995; Messenger 2000; Aléon et al. 2001; Floss et al. 2006; Busemann et al. 2009; Starkey and Franchi 2013), suggesting that the IDPs retain material from the interstellar medium (ISM), and may have escaped significant parent-body processing. The amount of carbon in IDPs is estimated to be around 10 wt% (Schramm et al. 1989) and most of it is reported to be amorphous in nature. It has been suggested that the amorphous carbon in IDPs that display very low G band positions compared with amorphous carbon in meteorites could be produced by ion irradiation in space (Ferini et al. 2004; Nittler et al. 2006). Very low G band positions are also observed in cometary material returned by the Stardust mission (Sandford et al. 2006; Rotundi et al. 2008).

To better understand the contributions of ISM material and ion irradiation to the properties of the

organic material in IDPs, it is important to assess the extent, if any, of parent-body processing the IDPs may have experienced. Low-temperature thermal processing is likely to erase or modify primary signatures in the IOM. However, IOM may be more chemically inert to aqueous alteration and, furthermore, it is not well understood how atmospheric entry heating may also affect the IOM (Cody and Alexander 2005; Busemann et al. 2007). The number of IDPs analyzed to date by Raman remains relatively small, particularly when the number of potential parent bodies is considered, or the huge volume of the protoplanetary disk that may have contributed to these parent bodies. This study seeks to compare the Raman parameters of the organic material in IDPs with the H, C, and N isotopic signatures on the same particles to help constrain the origin of the organic material.

In the past 10 years, it has been more common to use green wavelength (514 nm and 532 nm) lasers to investigate the organic matter in meteorites and IDPs (Quirico et al. 2003; Bonal et al. 2006b, 2007; Busemann et al. 2006, 2009; Dobrica et al. 2011). However, although shorter laser wavelengths (blue and green lasers) provide a high scattering intensity and spatial resolution, longer wavelengths associated with red lasers can be advantageous as they produce lower fluorescence with rock samples.

A few previous studies have focused on investigating various synthetic disordered and amorphous carbonaceous materials using a range of laser wavelengths (229–1064 nm) (Vidano et al. 1981; Wang et al. 1990; Ferrari and Robertson 2000, 2001). These multiple excitation wavelength studies (referring here to investigations employing the sequential use of a range of different monochromatic excitation sources, and hereafter referred to as "multiwavelength" studies) report dispersion in the Raman D and G band peak positions and intensities as a function of excitation wavelength, as well as variations in the properties of the Raman spectra as a function of the degree of ordering of the carbonaceous material. Multiwavelength Raman has not been applied systematically to document the dispersion of the carbon peaks from chondritic IOM, but it may offer additional information on the nature of the IOM and its variation between different types of samples. Dobrica et al. (2011) used both 532 nm and 244 nm laser wavelengths to study Antarctic micrometeorites. However, the 244 nm laser was only used on three samples, and primarily only to test for the presence of CN bonding rather than to compare the effects of dispersion with excitation wavelength. In a preliminary study of meteoritic IOM as part of an interlaboratory survey, Rotundi et al. (2008) observed dispersion in D band positions, and possibly also G band positions, as a function of laser wavelength.

This paper presents the results of a systematic, multiwavelength Raman study of IOM extracted from an extensive range of chondrites (including CV, CM, OC, CR previously studied by Alexander et al. [2007] and Busemann et al. [2007]) to document the dispersion of carbon peak parameters in the organic material present. Many experimental conditions are known to affect the measured Raman peak parameters (e.g., optical alignment, focusing laser power, medium between sample and detector and sample temperature [Busemann et al. 2007]). While it has not been possible to explore all of these different experimental conditions, the IOM suite we have analyzed is a representative sample of the IOM in the more primitive chondrites and provides a suitable reference with which to compare IDP samples that have been analyzed under identical conditions. IDPs cannot be classified by the conventional petrologic methods used for chondrites and so, Raman can potentially aid in the classification of IDPs. Raman has the added advantages of requiring virtually no sample preparation and, being relatively nondestructive, leaves the IDPs available for analysis by complementary techniques. The Raman IDP data presented here are also compared with other organic matter measurement indices, such as H, C, and N isotopic ratios acquired on the same particles.

METHODS

Meteoritic IOM Samples

The IOM samples employed in this study are from a diverse range of chondrite groups (CV, CM, CR, OC; see Tables 1 and 2 for more information) that cover a range of alteration indices. The IOM residues were produced for the study of Alexander et al. (2007) by demineralization of the bulk meteorites with CsF-HF dissolution (Cody et al. 2002; Cody and Alexander 2005). These residues have also previously been studied by Raman spectroscopy by Busemann et al. (2007) with a single laser excitation wavelength of 532 nm. For the Raman measurements in this study, the IOM was dispersed onto glass slides and analyzed without pressing. This approach is identical to the sample preparation employed by Busemann et al. (2007) and at least several of the studies involved in the comparative multiple laboratory investigation of Rotundi et al. (2008).

IDP Samples

Eighteen fragments from a total of nine large cluster IDPs were selected from the collection of IDPs

Table 1. Classification for IOM samples analyzed in this study, as taken from Alexander et al. (2007). Petrologic types for CVs are from Bonal et al. (2006a), for CMs are from Rubin et al. (2007), and for CRs from Abreu and Brearley (2010).

Meteorite	Find/Fall	Classification	Petrologic type	Shock	Weathering
CV ox					
Kaba	Fall	CV3 oxB	3.1	S1	
Mokoia	Fall	CV3 oxB	3.6	S1	
Bali	Fall	CV3 oxB	3.6	S2	
Allende	Fall	CV3 oxA	>3.6	S1	
CV red					
Leoville	Find	CV3 Red	3.1–3.2	S3	
Vigarano	Fall	CV3 Red	3.1–3.3	S1-2	
Efremovka	Find	CV3 Red	3.1–3.4	S4	
MET 01017	Find	CV3 Red			
CM					
Bells	Fall	CM2		S1	
Murchison	Fall	CM2	2.5	S1-2	
Murray	Fall	CM2	2.4/2.5	S1	
Cold Bokkeveld	Fall	CM2	2.2	S1	
ALH 83100	Find	CM1/2	2.1		Be
MET 01070	Find	CM1	2.0		Be
QUE 97990	Find	CM2	2.6		Be
CR					
MET 00426	Find	CR2	3.00		B
QUE 99177	Find	CR2	3.00		Be
EET 92042	Find	CR2			B
GRA 95229	Find	CR2			A
GRO 95577	Find	CR1			B
LEW 85332	Find	CR?			B/C
OC					
QUE 97008	Find	L3.05		S2	A
ALH 83010	Find	L3.3			B
GRO 95502	Find	L3.2		S2	B
Tieschitz	Fall	H/L 3.6		S3	
WSG 95300	Find	H3.3			A/B
Krymka	Fall	LL3.2			

at the Cosmic Dust Laboratory (CDL) at NASA Johnson Space Center. Cluster particles are fragile agglomerates of dust that fragmented into smaller pieces on contact with the silicone oil on the stratospheric collector. Sample details, including collector and cluster number, can be found in Table 3. The particles were placed on glass slides and rinsed with hexane to remove silicone oil. The Raman measurements were performed on the IDPs while still on the glass slides. The samples were then pressed flat into gold foil for SEM and NanoSIMS analyses. Numbers after IDP name (e.g., Lumley1, Lumley2) indicate that they are separate fragments picked from the same cluster particle at the CDL, and a letter after the number (e.g., Pevensey1a, Pevensey1b, etc.) indicates that an individual fragment broke apart into even smaller pieces when picking and pressing particles at The Open University.

Raman Measurements

The Raman measurements on the IDPs and meteoritic IOM were performed at the Open University using a HORIBA Jobin Yvon HR800 system equipped with 473 nm (blue diode), 514 nm (green argon ion), and 632 nm (red HeNe) excitation lasers. Some analyses using a 632 nm (red HeNe) excitation laser were performed at HORIBA UK Limited on an identical instrument, except that it was fitted with a Horiba Scientific Open Electrode Synapse CCD detector that gave an improved detection sensitivity for the red laser. Measurements were required on the HORIBA UK instrument for some of the IOM due to an "etaloning" problem with the CCD on the Open University system that resulted in a small ripple effect superimposed onto the spectra. This meant that some samples (with low signal resulting in apparent larger ripples) did not

Table 2. Raman parameters for meteoritic IOM and IDPs measured by blue (473 nm)$^{+}$, green (514 nm), and red (632 nm) lasers. All numbers are given as cm^{-1} representing the Raman shift relative to the excitation wavelength.

	D band	1σ	G band	1σ	D width	1σ	G width	1σ	D amp	1σ	G amp	1σ	ID/IG
BLUE 473 nm													
CVs													
Allende	1363.6	0.6	1599.0	1.4	73.4	2.9	66.6	1.8	174.8	28.0	122.5	20.1	1.4
Mokoia	1360.7	1.1	1604.4	1.1	95.6	2.4	55.4	1.7	186.3	49.7	174.9	48.8	1.1
Efremovka	1368.5	2.6	1599.1	2.1	189.7	9.9	82.6	6.5	97.3	14.1	98.4	13.4	1.0
MET 01017	1361.9	1.5	1592.8	1.9	77.5	7.6	59.2	8.3	100.8	24.5	104.3	29.1	1.0
Bali	1360.7	0.6	1603.2	1.0	97.9	3.3	58.1	1.6	200.3	30.0	182.1	27.2	1.1
Leoville	1366.2	0.8	1598.3	2.1	199.7	12.8	84.1	4.6	151.2	21.2	156.8	22.9	1.0
Vigarano	1363.1	1.1	1603.2	1.5	141.7	6.6	71.0	2.5	104.5	31.1	104.1	29.1	1.0
Kaba	1359.1	1.0	1602.6	1.5	172.0	3.8	63.2	1.8	232.0	43.6	274.6	50.6	0.8
CM													
QUE 97990	1367.0	2.0	1599.2	1.6	292.1	13.9	91.6	1.9	355.6	80.4	413.5	53.4	0.9
Murray	1363.5	2.3	1597.8	0.6	246.3	10.5	91.6	1.8	124.0	37.3	154.2	62.2	0.8
ALH 83100	1367.0	2.2	1599.5	1.0	241.8	14.2	90.7	2.0	124.2	64.7	162.4	109.9	0.8
MET 01070	1360.1	1.6	1596.6	1.2	271.8	9.4	87.6	2.3	543.4	98.3	653.7	123.2	0.8
Cold Bokkeveld	1365.1	1.1	1597.2	0.9	245.7	6.3	92.1	2.0	244.1	66.4	306.8	82.0	0.8
Murchison	1364.8	0.8	1596.2	2.4	246.5	28.5	96.8	1.5	179.0	42.1	212.5	55.7	0.8
Bells	1381.4	3.0	1596.9	1.1	242.1	14.6	86.5	3.2	381.3	82.6	472.3	98.8	0.8
OC													
QUE 97008	1370.5	3.9	1602.0	1.5	271.0	8.6	73.0	2.7	199.2	33.1	261.8	40.5	0.8
ALH 83010	1370.0	2.8	1589.8	1.8	150.8	24.6	83.4	9.9	88.0	19.7	104.0	22.5	0.8
GRO 95502	1360.2	0.7	1602.4	1.6	156.1	15.4	68.0	2.1	159.9	30.6	171.0	32.1	0.9
Tieschitz	1364.4	1.2	1602.1	1.3	125.4	3.9	70.9	2.2	132.8	37.8	127.3	35.8	1.0
WSG 95300	1363.6	0.5	1599.0	2.0	168.5	15.8	78.5	2.8	116.0	42.3	125.1	44.6	0.9
Krymka	1364.7	1.4	1601.7	0.8	184.5	16.0	76.4	1.3	136.0	45.4	150.3	46.6	0.9
CRs													
EET 92042	1375.4	3.8	1597.9	1.8	288.3	7.9	91.2	2.5	477.8	102.5	613.6	158.4	0.8
GRO 95577	1365.2	2.7	1595.1	1.3	281.9	12.2	88.8	2.3	411.6	71.2	476.2	173.6	0.9
GRA 95229	1369.3	4.4	1595.2	1.0	263.7	21.6	95.1	3.9	446.7	220.6	532.8	291.8	0.8
MET 00426	1373.8	3.2	1596.3	1.8	289.5	12.9	92.1	2.4	384.2	79.4	448.7	128.6	0.9
QUE 99177	1369.8	2.9	1594.8	1.1	294.1	16.6	90.1	3.7	468.3	103.7	559.7	124.5	0.8
LEW 85332	1371.3	3.1	1595.0	0.9	295.2	9.2	92.9	2.0	343.5	104.1	399.6	141.3	0.9
GREEN 514 nm													
CVs													
Allende	1352.2	0.5	1600.1	1.1	85.9	3.4	68.2	1.1	168.5	24.2	115.6	30.5	1.5
Mokoia	1344.9	0.4	1600.3	0.4	100.8	1.9	53.9	1.3	167.9	36.4	155.6	33.6	1.1
Efremovka	1350.5	1.8	1593.1	1.4	200.7	9.2	82.3	3.5	136.5	20.4	129.4	19.6	1.1
MET 01017	1349.2	1.3	1587.3	2.6	72.5	13.6	50.0	10.9	82.8	24.3	98.0	17.1	0.8
Bali	1347.1	0.4	1599.8	0.7	105.9	2.8	58.0	1.3	220.4	33.3	196.6	30.6	1.1
Leoville	1353.0	0.8	1593.1	1.3	215.3	13.3	86.0	3.1	149.8	33.1	140.0	31.1	1.1
Vigarano	1348.2	0.9	1596.8	2.3	155.0	15.8	71.5	4.2	120.3	43.5	119.3	43.1	1.0
Kaba	1344.3	0.8	1598.7	0.9	184.7	4.4	63.2	1.2	257.6	44.7	291.2	49.7	0.9
CM													
QUE 97990	1356.8	3.4	1592.8	1.2	310.1	12.5	91.5	3.0	800.6	100.0	851.5	134.0	0.9
Murray	1354.0	2.2	1595.2	0.7	283.2	9.5	91.1	2.7	507.0	74.8	552.5	93.4	0.9
ALH 83100	1354.0	2.1	1595.1	1.2	286.9	11.1	88.4	3.3	711.5	145.9	781.1	177.8	0.9
MET 01070	1348.3	1.8	1595.7	0.9	279.4	8.1	87.6	2.0	572.2	119.7	672.8	142.5	0.9
Cold Bokkeveld	1352.1	1.4	1592.8	1.1	279.6	10.7	91.8	2.3	362.1	27.1	389.0	26.5	0.9
Murchison	1358.0	1.7	1593.9	1.2	274.2	18.7	90.4	2.6	241.8	75.9	310.8	89.4	0.8
OC													
QUE 97008	1358.6	3.7	1597.1	1.5	277.4	8.2	75.8	3.0	202.5	30.4	231.2	38.9	0.9
ALH 83010	1357.9	1.4	1589.7	1.3	137.5	42.1	81.9	13.3	63.9	11.1	65.2	10.3	1.0
GRO 95502	1348.4	4.7	1599.7	1.2	160.3	20.8	66.9	5.2	136.0	16.3	139.2	28.6	1.0

Table 2. *Continued*. Raman parameters for meteoritic IOM and IDPs measured by blue (473 nm)+, green (514 nm), and red (632 nm) lasers. All numbers are given as cm^{-1} representing the Raman shift relative to the excitation wavelength.

	D band	1σ	G band	1σ	D width	1σ	G width	1σ	D amp	1σ	G amp	1σ	ID/IG
Tieschitz	1349.7	0.5	1598.0	0.7	139.3	6.9	73.6	1.5	158.0	15.5	143.6	15.0	1.1
WSG 95300	1350.9	0.9	1597.4	1.4	160.9	11.3	75.0	2.1	102.3	27.1	100.7	26.5	1.0
Krymka	1349.1	0.8	1597.4	0.8	197.0	5.5	75.7	1.5	205.5	17.8	208.9	19.8	1.0
CRs													
EET 92042	1362.0	3.6	1593.5	1.7	318.3	17.7	91.4	4.0	790.2	107.5	877.9	121.5	0.9
GRO 95577	1356.9	2.0	1594.4	0.5	297.9	8.2	87.1	1.3	861.0	145.7	997.9	147.0	0.9
GRA 95229	1362.6	2.8	1594.9	0.5	295.2	11.8	103.6	3.7	903.0	100.5	1011.4	108.5	0.9
MET 00426	1366.1	2.2	1594.0	0.8	313.7	11.3	95.3	2.4	959.1	30.4	1136.8	53.6	0.8
QUE 99177	1362.1	1.9	1594.9	1.9	301.8	6.8	89.1	4.3	518	178.4	592.8	209.8	0.9
LEW85332	1362.7	2.5	1594.8	0.7	297.3	10.0	90.2	1.4	699.8	104.7	805.6	114.1	0.9
IDPs													
Bramber1	1364.3	3.2	1583.2	0.6	306.0	5.3	119.7	1.6	332.3	100.5	302.9	28.7	1.1
Pevensey2	1353.6	2.5	1587.1	0.9	265.5	6.8	116.2	2.2	200.0	105.6	184.4	124.2	1.1
Midford2	1360.1	1.7	1587.8	1.1	286.1	10.7	102.6	4.1	579.7	76.9	628.5	108.7	0.9
Arundel1	1364.0	3.7	1589.2	1.0	283.1	8.2	116.1	4.5	89.2	99.4	84.4	87.6	1.1
RED 632 nm													
CVs													
Allende	1331.6	0.3	1603.0	0.2	77.6	1.0	56.2	1.1	46.1	2.6	23.5	1.1	2.0
Efremovka	1330.4	0.8	1595.0	0.7	202.2	5.6	86.1	2.0	226.1	37.4	166.9	27.9	1.4
MET 01017	1331.6	1.4	1593.2	2.2	74.1	8.3	61.7	5.5	171.1	29.7	123.4	19.6	1.4
Leoville	1334.2	1.8	1596.6	1.6	188.7	13.1	84.5	2.8	419.1	36.9	325.6	29.0	1.3
Kaba	1330.2	0.6	1600.5	0.6	174.2	2.8	64.3	1.1	523.7	39.7	469.1	33.7	1.1
CM													
QUE 97990*	1341.1	2.6	1588.4	1.6	316.0	17.2	101.0	4.7	509.8	111.7	362.1	97.4	1.4
Murray*	1338.4	3.8	1588.6	0.8	297.2	9.0	104.5	7.6	541.5	66.5	398.2	57.6	1.4
ALH 83100*	1338.3	1.1	1589.4	0.9	290.5	12.4	96.8	2.7	407.3	75.1	295.0	55.1	1.4
MET 01070*	1337.5	1.6	1591.1	1.1	300.1	18.0	96.0	3.2	303.5	148.7	227.0	136.0	1.3
Cold Bokkeveld	1342.0	1.5	1589.9	1.0	241.8	17.5	107.2	4.5	262.2	85.8	193.6	64.8	1.4
Murchison	1336.7	2.1	1588.8	1.4	299.6	9.6	99.5	5.1	377.5	46.2	272.7	34.1	1.4
OC													
QUE 97008	1337.9	1.0	1597.8	1.6	290.3	11.5	80.6	3.3	261.5	62.9	203.9	52.6	1.3
ALH 83010	1335.3	2.8	1594.2	3.3	169.1	23.9	90.6	10.0	79.8	26.1	58.7	18.5	1.4
GRO 95502	1330.7	0.8	1601.5	0.6	156.5	6.4	66.6	1.6	308.1	58.5	242.2	47.4	1.3
CRs													
EET 92042*	1344.6	2.1	1595.0	1.6	286.4	14.5	107.6	6.2	595.9	35.2	469.6	52.9	1.3
GRO 95577*	1342.4	1.5	1595.8	2.5	304.3	35.9	117.4	20.2	399.5	99.1	349.0	64.7	1.1
GRA 95229*	1344.9	2.8	1595.0	4.8	296.6	44.6	127.7	13.1	494.8	51.6	403.1	44.4	1.2
MET 00426*	1344.6	2.3	1594.8	2.3	300.3	28.3	116.6	4.3	373.0	78.2	318.7	52.3	1.2
QUE 99177*	1342.5	1.8	1592.4	4.2	288.8	28.5	109.7	5.1	592.8	82.7	467.2	68.5	1.3
LEW 85332*	1345.0	1.4	1594.1	1.2	297.8	7.4	106.5	5.2	374.8	106.5	289.2	105.8	1.3
IDPs													
Bramber1	1343.9	1.1	1582.1	2.5	337.2	14.6	128.0	7.6	141.3	45.8	87.2	20.3	1.6
Pevensey2	1338.3	2.9	1586.0	1.6	295.3	36.8	121.9	9.8	132.9	25.7	88.5	63.8	1.5
Midford2	1340.3	1.1	1585.5	3.2	321.3	11.6	102.2	5.2	663.9	84.6	467.2	44.6	1.4

*Red laser data collected at HORIBA, UK.

+Blue (473 nm) results for IDPs studied by all three wavelengths are presented in Table 3 along with all blue (473 nm) IDP results.

produce reliable spectra that could be accurately fitted. In comparison to tests using samples with a high signal-to-ripple ratio, no statistical differences were observed between results from the two instruments. Reliable spectra were, therefore, obtained at HORIBA UK for most of the samples that were not analyzed with the Open University red laser system, although red laser data were not obtained for all of the samples in the time available (see Table 2).

Raman analyses of IOM and IDPs were obtained as maps of point spectra with step sizes of between 1 and 2 μm in both the x and y directions. The autofocus

Table 3. Raman parameters for IDPs measured by blue (473 nm) laser. All numbers are given as cm^{-1} representing the Raman shift relative to the excitation wavelength.

IDP fragment name*	Collector Cluster #	D band	1σ	G band	1σ	D width	1σ	G width	1σ	I(D)/I(G)
Starkey2	L2009 Cluster14	1366.6	2.2	1593.8	1.5	251.1	9.7	109.5	1.5	0.9
Alnwick1	L2009 Cluster14	1367.5	3.1	1585.4	1.7	273.5	12.0	118.8	6.3	0.8
Alnwick2	L2009 Cluster14	1367.8	1.7	1582.2	1.3	271.2	8.6	128.8	6.5	0.8
Dunster1	L2071 Cluster23	1367.3	3.5	1586.4	1.9	296.6	11.2	111.7	3.9	0.8
Balmoral1	L2071 Cluster2	1370.1	3.0	1585.3	1.4	286.1	16.4	114.8	6.2	0.9
Lumley1	L2009 Cluster10	1370.1	3.4	1587.4	1.1	291.7	14.3	110.2	3.0	0.8
Lumley2	L2009 Cluster10	1364.7	2.6	1590.1	3.5	279.6	27.2	103.7	6.7	0.8
Pevensey 1a	L2005 Cluster12	1371.4	3.4	1588.9	2.2	280.0	20.6	113.4	4.7	1.1
Pevensey 1b	L2005 Cluster12	1369.0	3.7	1593.2	1.5	250.1	16.6	110.4	4.7	1.1
Pevensey2a	L2005 Cluster12	1370.7	3.9	1593.0	2.0	269.0	25.1	112.3	5.0	1.0
Pevensey2b	L2005 Cluster12	1370.7	4.0	1593.0	1.3	266.8	17.6	111.3	5.2	1.0
Pevensey 3	L2005 Cluster12	1374.7	7.1	1589.4	4.4	278.8	34.6	109.3	7.2	1.2
Arundel1	L2005 Cluster15	1373.6	5.8	1593.9	3.4	283.8	40.0	104.7	10.9	1.4
Bramber1	L2006 Cluster4	1373.2	3.9	1587.8	2.0	301.0	11.5	114.4	3.9	1.1
Bramber2	L2006 Cluster4	1374.5	6.0	1583.3	2.0	302.2	14.1	116.5	4.2	1.1
Bramber4	L2006 Cluster4	1368.9	3.6	1587.3	1.5	276.2	20.2	111.1	2.5	0.9
Midford1	L2006 Cluster14	1366.8	3.1	1595.3	1.8	276.2	23.1	91.0	4.1	0.8
Midford2	L2006 Cluster14	1368.1	5.0	1590.4	1.9	296.9	25.5	100.2	5.1	0.9

*Cluster particles are named after castles situated in the United Kingdom.

function was used for these analyses because the IOM and IDPs did not have flat surfaces as they were not crushed. The autofocus procedure was applied prior to every point spectrum based on maximum Raman signal at approximately 1590 cm^{-1}. Individual spectra (i.e., those obtained at each point on the map) were accumulated as four sets of 10 s integrations across particles on glass slides. For some IDPs, longer analyses were necessary (four sets of 30 s integrations) to improve the signal-to-noise ratio. A low laser power of <70 μW at the sample surface was maintained throughout all measurements, so that thermal damage to the sample was minimized (see Busemann et al. 2007; Rotundi et al. 2008). A × 50 long working distance objective lens giving a spot size of approximately 2 μm was used. Spectra were obtained with a 600 mm grating and 800 mm focal length spectrometer giving a spectral resolution of approximately 3 cm^{-1}. The spectral range was calibrated using a silicon standard at the beginning of each analytical session. First order carbon D and G bands were fitted in the range 800–2100 cm^{-1}, assuming a linear baseline and Gaussian-Lorentzian peak shapes. In an interlaboratory study carried out by Rotundi et al. (2008), it was found that the different peak-fitting procedures, including Gaussian-Lorentzian and Lorentzian fitting, used by five different laboratories to fit bands to synthetic and real IOM spectra did not add any systematic errors to measurements. The Raman band parameters are presented as wave numbers (cm^{-1}) representing the Raman shift relative to the exciting laser wavelength. The peak positions for the D and G bands, their peak widths (measured at the full width half-maximum), and the intensities of the D versus the G bands (I(D)/I(G)) were obtained for each IDP by averaging the peak parameters from all spectra obtained from each particle (minimum number of spectra obtained per sample was 15). The uncertainties are reported as the standard deviation of the mean values from each sample (1σ). Individual point analyses within a map that showed an unsuitable fit for the baseline (i.e., baselines that showed a large variation across the spectrum) were eliminated. Due to low fluorescence in most analyses, a good spectral fit was achieved in well over 95% of point analyses. This approach is similar to that set out by Rotundi et al. (2008).

All IOM samples included in this study were measured with the 473 nm (blue) and 514 nm (green) excitation lasers, and all except four samples with the 632 nm (red) laser. Four IDPs were also measured at multiple excitation wavelengths (Bramber1, Pevensey2, Midford2, and Arundel1). The remaining 15 IDPs were only analyzed with the blue (473 nm) laser. The analyses were completed over a period of 1 year and, in addition to daily calibration procedures, a sample of Allende IOM was used to verify the overall performance of the instrument regularly during each set of measurements. The measurement of Allende IOM and the subsequent spectral fitting procedure showed a good reproducibility over this time.

NanoSIMS Measurements

All the IDPs in this study, except for the fragments from the IDP Pevensey cluster, were analyzed for H, C,

Table 4. H, C, and N isotopic data for those samples measured as part of this study. All other IDP isotope data are available in Starkey and Franchi (2013).

IDP fragment name	$\delta D‰$	$\delta D‰$ 2σ	$\delta^{13}C‰$	$\delta^{13}C‰$ 2σ	$\delta^{15}N‰$	$\delta^{15}N‰$ 2σ	C/H
Starkey2	1256	88	−34	5	80	4	1.1
Alnwick1	566	61	−35	3	271	5	1.0
Alnwick2	710	59	−30	2	291	4	0.9
Dunster1	1406	106	−25	2	355	4	1.6
Balmoral1	1095	67	−26	4	228	9	1.1
Lumley1	709	67	−15	4	303	6	1.1
Lumley2	1084	64	−29	3	223	5	0.9
Bramber4	273	37	−43	7	385	9	0.5
Bramber5	1394	35	−26	3	209	4	1.6

and N isotopes by NanoSIMS after Raman analyses were completed to avoid any anomalous behavior associated with ion beam damage. For the IDPs Midford1, Midford2, Bramber1, Bramber2, Arundel1, and Arundel3, the isotopic data are available in Starkey and Franchi (2013). For the IDPs Alnwick1, Alnwick2, Dunster1, Balmoral1, Lumley1, Lumley2, and Bramber4, the isotopic data are presented here for the first time (Table 4), but were analyzed using the same methodology as described in Starkey and Franchi (2013), and summarized below.

The IDPs were analyzed in NanoSIMS imaging mode for H, C, and N isotopes (further details in Starkey and Franchi 2013). In all cases, the negative secondary ions were collected on electron multipliers. Each of the IDPs were analyzed in two sessions: in the first, ^{12}C, ^{13}C, ^{16}O, $^{12}C^{14}N$, $^{12}C^{15}N$, and ^{28}Si were collected simultaneously, and in the second, ^{1}H, ^{2}H, and ^{12}C were collected simultaneously. A Cs^+ primary ion beam with a current of 1.5 pA was used for the C and N isotope measurements, and a 3 pA primary beam was used for the H isotope analyses. The primary ion beam was rastered over the samples with an analytical raster size around 2 μm in both axes larger than the particle, and a presputter raster size around 5 μm larger. In both cases, the probe size was typically ≤150 nm, and the raster image maps were made with a pixel step size of ≤100 nm with dwell times of 1000 μs per pixel. Forty planes of data were collected for each sample, giving total analysis times of approximately 40 min. The planes of image data were corrected for detector deadtime, then combined, aligned, and processed using the L'image software (L. Nittler, Carnegie Institute of Washington) to provide bulk $\delta^{13}C$, $\delta^{15}N$, δD, and C/H ratios for each IDP by taking total ion yields for each particle, although it is noted that this may not provide perfect bulk values because of variable ion yields from different phases. Data were corrected for IMF (instrumental mass fractionation) and normalized to isotopic and elemental ratios relative to analyses of Cold Bokkeveld IOM during the analytical run. While Cold Bokkeveld IOM is not homogeneous and, therefore, may not represent the perfect standard, it was selected as a good elemental match for organic matter in IDPs. Pressed particles of Cold Bokkeveld IOM were analyzed over a 1-year period with the variations observed in the bulk ratios being small (e.g., $^{13}C/^{12}C \pm 8‰$, $^{15}N/^{14}N \pm 20‰$, $^{2}D/^{1}H \pm 60‰$), in comparison to those observed for the same ratios in the IDPs. The variation observed between Cold Bokkeveld IOM analyzed during any one setup was very small (e.g., for $^{13}C/^{12}C$ 1–2‰, which is within counting statistics). Internal heterogeneities caused by the effects of hotspot abundance in the Cold Bokkeveld IOM were assessed by isotopic mapping and found to be minimal. Typically, for a single pressed grain of Cold Bokkeveld IOM, the bulk particle will contain approximately 5% $^{13}C/^{12}C$ and 5% $^{15}N/^{14}N$ hotspots (hotspots include +ve and −ve anomalies). The average composition of the hotspot regions is only a few tens of permil different from the bulk particle for C and N isotopes. The δD hotspots are all enriched in D in Cold Bokkeveld, representing only approximately 2% of the bulk particle (with an average isotopic composition of approximately 3000‰), which, therefore, contributes a few tens of permil to the total isotopic composition.

RESULTS AND DISCUSSION

Typical spectra obtained from IOM samples from CR, CM, CV, and OC meteorites are shown in Fig. 1. All samples provided good spectra, with sufficiently high signal to noise to enable good peak fitting. The fluorescence background was variable between, and even within, samples, and was generally higher for the CR and CM samples than for the CV and OC samples. However, the fluorescence background was rarely greater than twice the G band amplitude, and therefore could be readily accounted for during peak fitting. Typical spectra from the IDPs are also shown in Fig. 1, and demonstrate

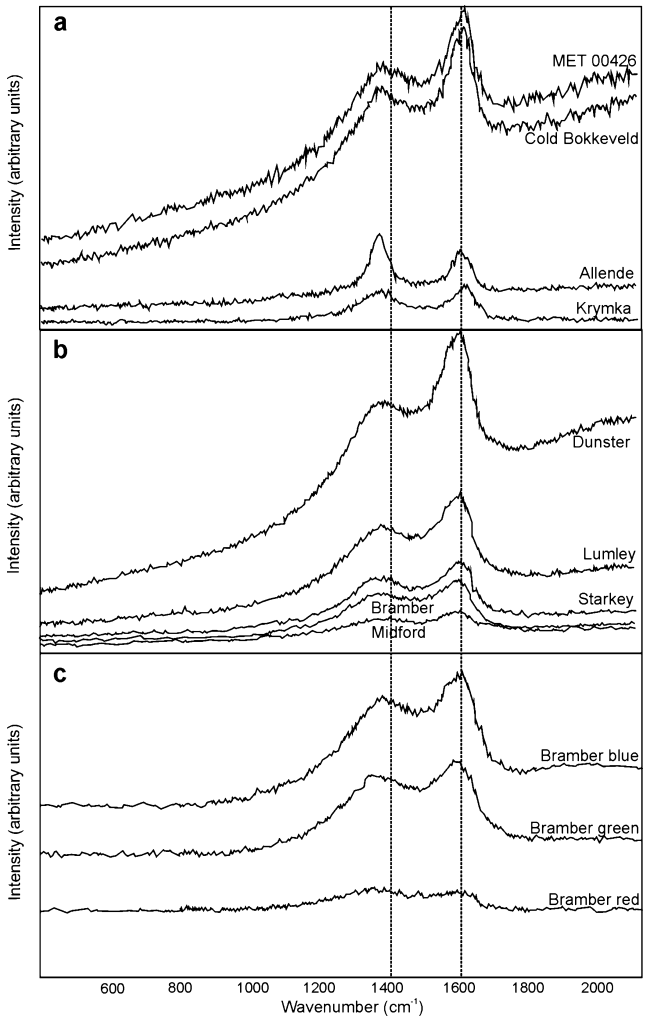

Fig. 1. Examples of typical spectra for a) IOM using 473 nm (blue) laser; b) IDPs using 473 nm (blue) laser; c) IDP Bramber using blue (473 nm), green (514 nm), and red (632 nm) lasers.

similar levels of signal-to-noise, and peak-to-background ratios as the IOM, although, because of the more complex composition of the IDPs (i.e., variable levels of silicate matrix in addition to organics), there was greater variation in the spectra from these samples.

Multiwavelength Raman Variations within Meteorite Groups

The results for the IOM D and G band properties determined for each excitation wavelength are shown in Table 2 and Fig. 2. It is observed that D and G band positions of the IOM generally decrease with increasing excitation wavelength and that the decreases are much larger for the D band position than that of the G band (Figs. 2a–d). However, it should be noted that the G band itself is a "hybrid" band composed of the true G band along with the overlapping, but unresolved, D′ band. It is, in fact, more likely that it is the disorder-induced D′ band that shows the dispersion observed here, rather than the true G band itself, which cannot show dispersion.

When considering the IOM data for each excitation wavelength as a whole, the average for the D band positions are 1366.3 cm^{-1} (473 nm), 1353.8 cm^{-1} (514 nm), and 1338.0 cm^{-1} (632 nm). The average G band positions for each excitation wavelength are 1598.4 cm^{-1} (473 nm), 1595.4 cm^{-1} (514 nm), and 1594.2 cm^{-1} (632 nm). Although the differences between the average G band positions obtained by the different lasers are small compared with the range of G band positions as a whole, there are clear offsets in the trends obtained from these three lasers (Fig. 2d). The D bandwidths display a wide range of values and increase with increasing excitation wavelength from an average, for the IOM data set for each excitation wavelength taken as a whole, of 207.5 cm^{-1} (473 nm), 220.4 cm^{-1} (514 nm), and 242.6 cm^{-1} (632 nm), showing a fairly systematic increase. The G band widths of the meteoritic IOM also display a wide range of values at each excitation wavelength. The blue and green lasers provide very similar average G band-width values for each data set (82.2 cm^{-1} (473 nm) and 81.6 cm^{-1} (514 nm)), but with the 632 nm (red) laser average being somewhat higher (95.6 cm^{-1}). The results for both the G band position and width obtained using the red laser display a larger range than those obtained with the other two laser wavelengths and the reason for this is unclear at this point in time.

The Raman data obtained on the IOM with the 514 nm green laser in this study are compared with the results obtained on the same IOM residues in the study of Busemann et al. (2007) (Fig. 2) using a 532 nm laser on a different Raman system (a WiTec alpha-SNOM micro-Raman) to the one in this study. In the case of the D band, the IOM data of Busemann et al. (2007) fall generally, as expected, between the IOM measured in this study with the 514 nm and the 632 nm lasers.

However, to truly understand the reproducibility of the Raman data obtained in this study with the measurements obtained on the same IOM residues in the study of Busemann et al. (2007), the two data sets are directly compared on a single meteorite basis. The individual IOM measurements in this study for type 2s (CMs and CRs) and type 3s (CVs and OCs) provide contrasting correlations with the results from the same samples obtained by the study of Busemann et al. (2007) (Figs. 3a and 3b). The trends displayed between the two data sets for D and G band position, and D and G bandwidth (only D band parameters shown in Fig. 3) for the type 3 chondrites are conformable, with slopes of approximately 1. However, this is not the case

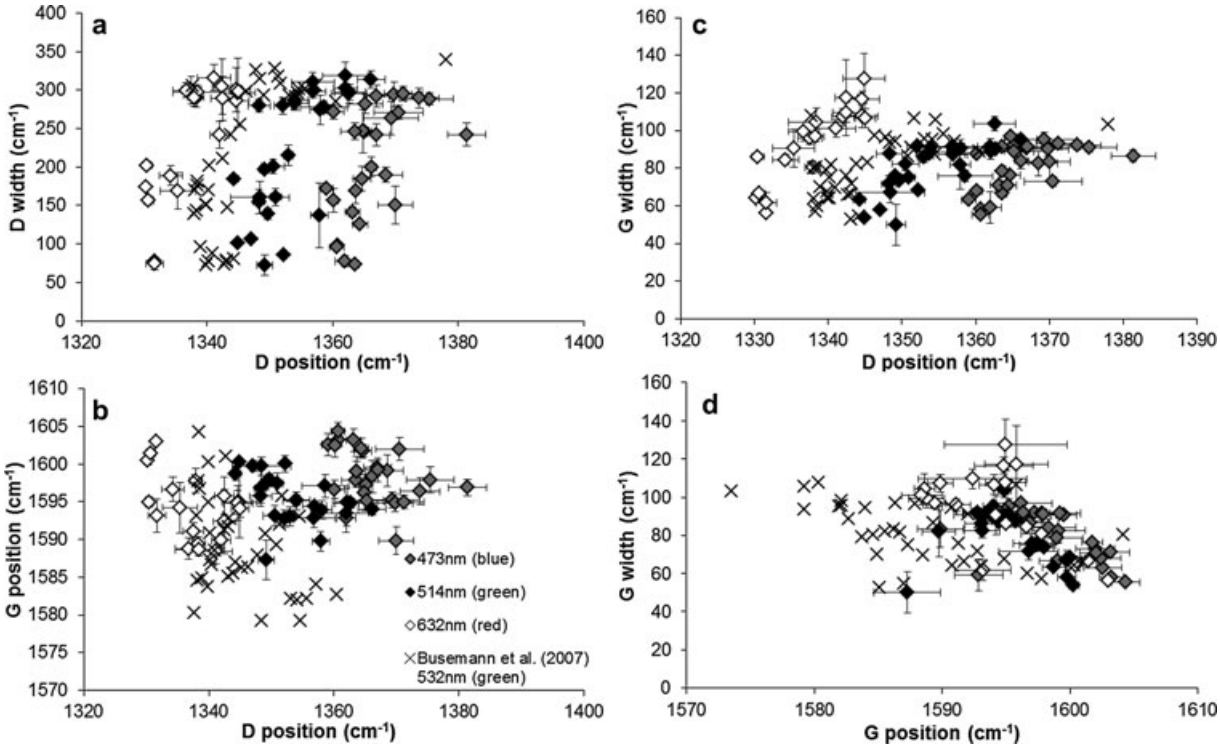

Fig. 2. a–d) D and G band parameters (given as cm^{-1} representing the Raman shift relative to the excitation wavelength) for Raman multiwavelength measurements (473 nm [blue] laser, 514 nm [green] laser, and 632 nm [red] laser) of IOM of this study. Included also are data from Busemann et al. (2007) obtained using a 532 nm (green) laser. The results of Busemann et al. (2007) that are shown include only samples of those meteorites also reported here. Error bars are shown as 1σ.

for the type 2 chondrites, where the Raman data obtained in the two studies do not appear to show any obvious relationships. A similar pattern is apparent in a comparison of the results obtained by the different lasers in this study: between the green and blue lasers (Fig. 3c), and the red and the green (Fig. 3d). The fact that the same IOM residues were used throughout, and between this study and the study of Busemann et al. (2007), means that the lack of correlation for the type 2 chondrites cannot be due to different sample preparations or instrument effects. However, because the IOM residue is dispersed as individual grains across a glass slide, it is highly unlikely that the same grain was measured repeatedly at all wavelengths (and definitely not between this study and that of Busemann et al. 2007). This observation suggests that the type 2 chondrite measurements may not be reproducible because the type 2 chondrite IOM is itself heterogeneous at the individual particle level. The conformability of the type 3 data not only confirms the reproducibility of the method but also that the organic matter in these meteorite groups is more homogenous at the individual particle level. These ideas are discussed further in the Meteoritic IOM—Unraveling the Raman Parameters to Understand the Organic Matter section.

Multiwavelength Raman Variations within IDPs

The measured G and D band peak positions as a function of excitation wavelength for meteoritic IOM and IDPs are displayed in Fig. 4. The slope of the lines, expressed as $cm^{-1}\ nm^{-1}$, indicates the amount of dispersion (Fig. 4), with the steeper slopes reflecting larger dispersion for the given Raman parameter. For all IOM and IDPs, the slopes for D band peak positions against increasing excitation wavelength are negative, and within each chondrite group, the individual meteorite trends are generally similar to each other—although some cross-cutting patterns are observed in some chondrite groups (type 2 chondrites more than type 3s). The dispersion slopes are approximately linear, although, in the case of the CV meteorites, the slope between the green and blue excitation wavelengths is consistently greater than that between the red and green excitation wavelengths. Several samples from other chondrite groups appear to display similar patterns (Fig. 4), but this may be the result of heterogeneity, or the uncertainty within the measurements. The OCs and CVs show the largest dispersion with average slopes that are steeper than $-0.2\ cm^{-1}\ nm^{-1}$, while the CRs and CMs display less negative slopes (less than $-0.17\ cm^{-1}\ nm^{-1}$), i.e., less

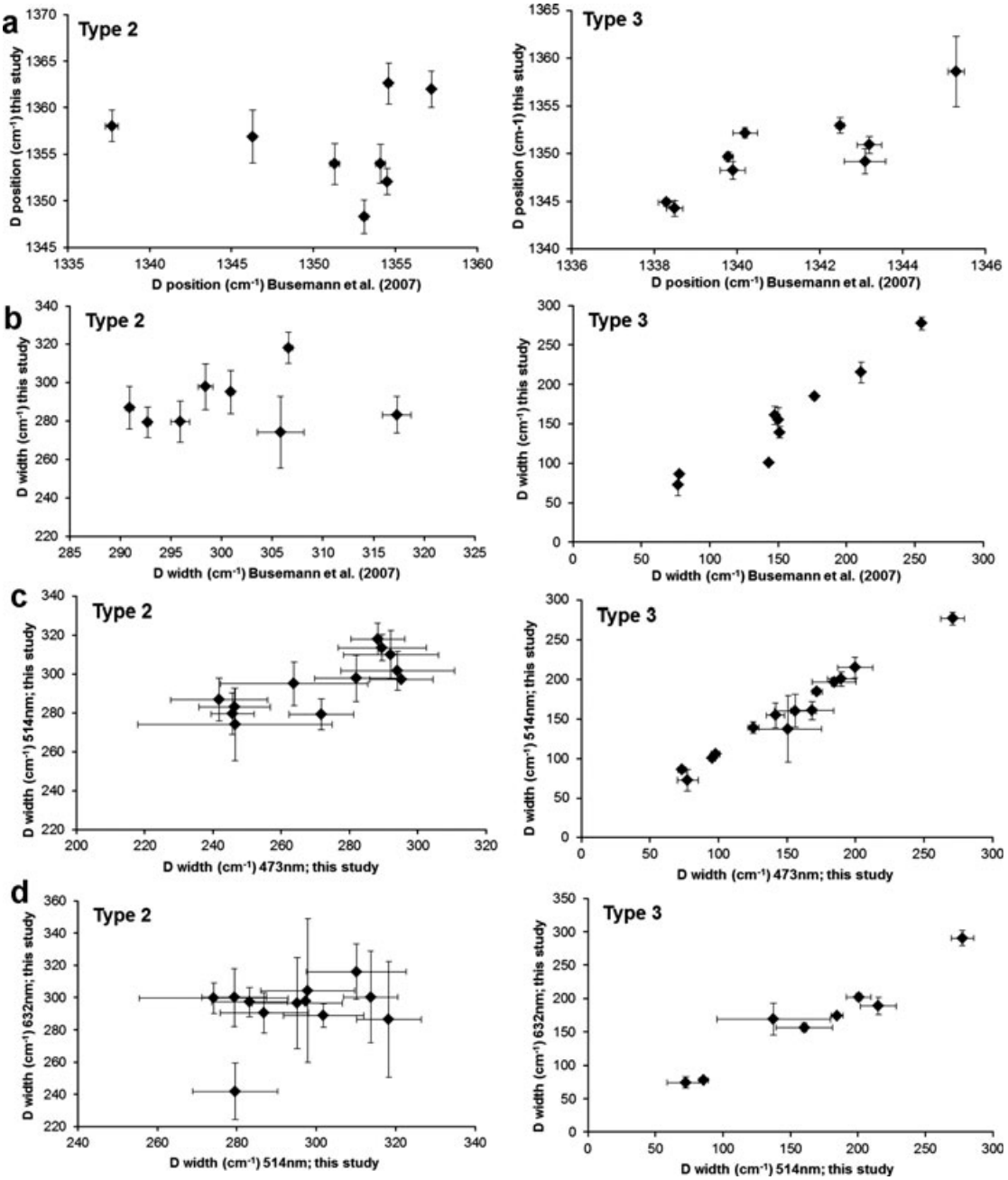

Fig. 3. Comparisons on an individual meteorite basis for data obtained at different excitation wavelengths on the same IOM residue. a) D band positions and b) D bandwidths for type 2 and type 3 chondrites measured by 514 nm green laser in this study compared with the same IOM measured in the study of Busemann et al. (2007) with a 532 nm laser. c) D bandwidths for type 2 and type 3 chondrites measured with 473 nm (blue) and 514 nm (green) laser in this study. d) D bandwidths for type 2 and type 3 chondrites measured with 514 nm (green) and 632 nm (red) laser in this study.

dispersion. The slope calculated for the IDPs (-0.18 cm^{-1} nm^{-1}) falls between that of the CMs and CRs, and that of the OCs.

The G band peak position dispersion is more variable than that of the D band peak position. This is most likely related to the "hybrid" nature of the G band, meaning that, in practice, what we measure is a mixed signal from the true G band and the unresolved overlapping D′ disorder-induced band. Ferrari and Robertson (2001) showed that the dispersion of the measured G band peak position generally increases over the wide range of excitation wavelengths in the amorphous carbonaceous materials that they tested. As with their D band peak parameters, the G band peak positions of the OCs and

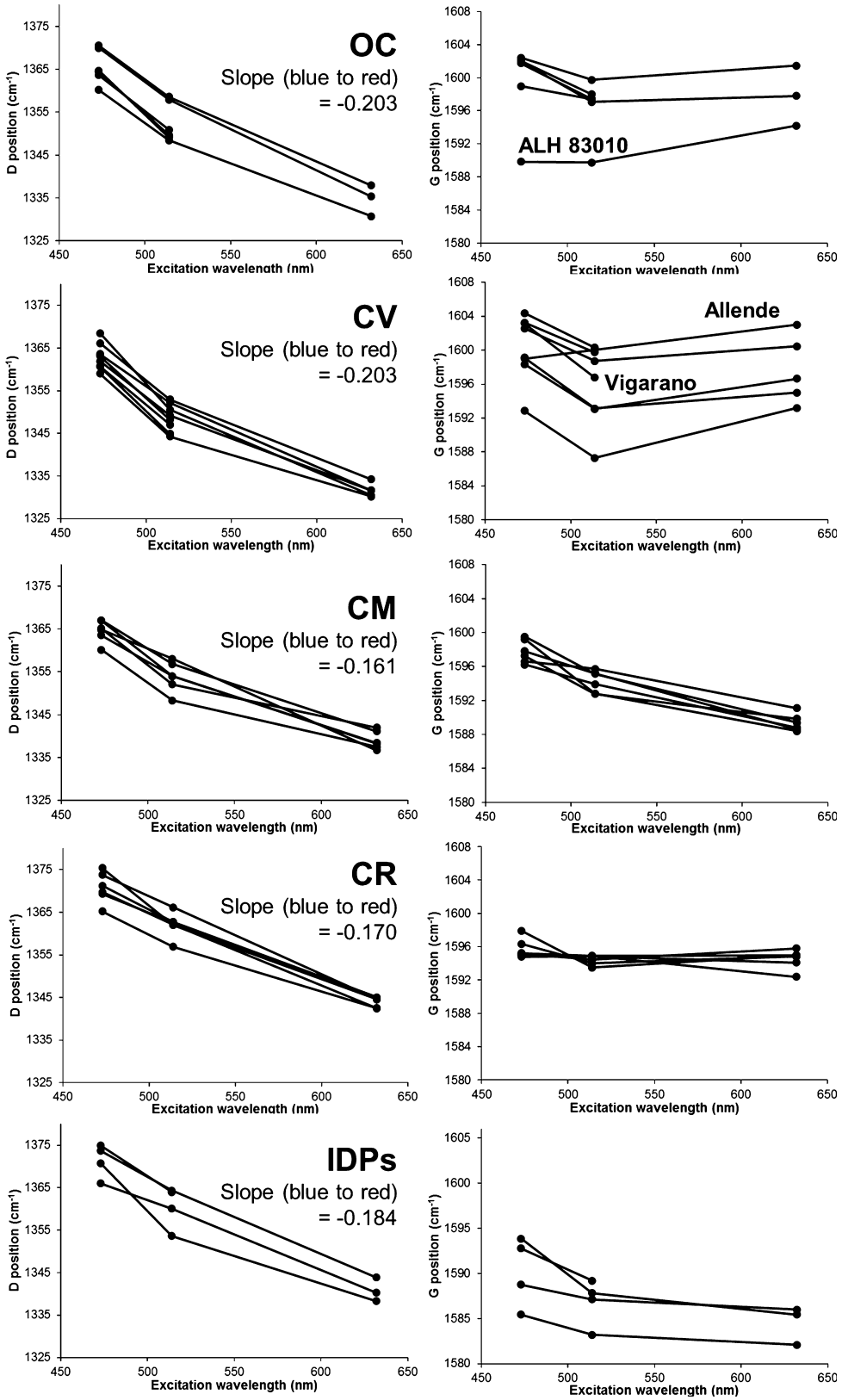

Fig. 4. Excitation wavelength against D and G peak positions (given as cm^{-1} representing the Raman shift relative to the excitation wavelength) for IOM from meteorite groups (OC, CV, CM, CR) and IDPs. Typical 1σ errors for all samples are indicated on the top panel. Slope (cm^{-1} nm^{-1}) indicates the dispersion of the D band as calculated between the 473 and 632 nm lasers.

CVs show similar patterns to each other (Fig. 4). However, in the case of the G band, the dispersion for each meteorite in these groups follows a "V"-shaped pattern—with similar G band positions determined using the blue (473 nm) and red (632 nm) lasers, while the G band positions measured using the green (514 nm) laser are consistently lower by up to 5 cm^{-1} (Fig. 4).

On the whole, the dispersion slopes displayed by the four IDPs measured with multiwavelength Raman in this study are similar to one another, and are broadly similar to those of the IOM in CMs and CRs. In the case of the D band peak position, the IDP dispersion is more similar to that displayed by IOM from the CRs rather than the CMs. On the other hand, the G band peak positions of the IDPs display some weak dispersion, while the CRs exhibit essentially none and the CMs show a slightly larger dispersion in the same direction, which is more similar to the IDPs.

These data confirm the relationship previously observed for synthetic amorphous carbonaceous material (Ferrari and Robertson 2000, 2001), that the Raman spectral parameters are affected not only by the type of carbon bonding present in the sample, but also by the excitation wavelength used for investigation. From the mean values obtained from the IOM samples, there does not appear to be a simple relationship between measured Raman parameters and excitation wavelength, and therefore it is not possible to suggest a simple correction factor that could be applied to account for the variations observed when IOM is measured with different excitation wavelengths.

Relationship between IOM and IDPs Measured at a Single Excitation Wavelength

The peak parameters for 18 individual IDP cluster fragments and the IOM samples measured with the blue laser (473 nm excitation wavelength) are compared in Fig. 5. As indicated by the IOM analyzed here, and demonstrated by Busemann et al. (2007), there is a general pattern of the type 2 chondrites having higher D band positions, higher D and G bandwidths, and lower G band positions than the type 3 chondrites. These trends indicate progressive ordering of the carbon with increasing metamorphic grade. The D band peak parameters determined from the IDPs display a range of peak widths and positions that are indistinguishable from those determined for CM and CR IOM. None of the IDPs fall to the very low D bandwidth values that are observed for the more metamorphosed IOM, indicating that ordering of the organic carbon during atmospheric entry was limited in these particles, or that kinetic controls on the rate of ordering meant that heating is not apparent in the Raman signatures.

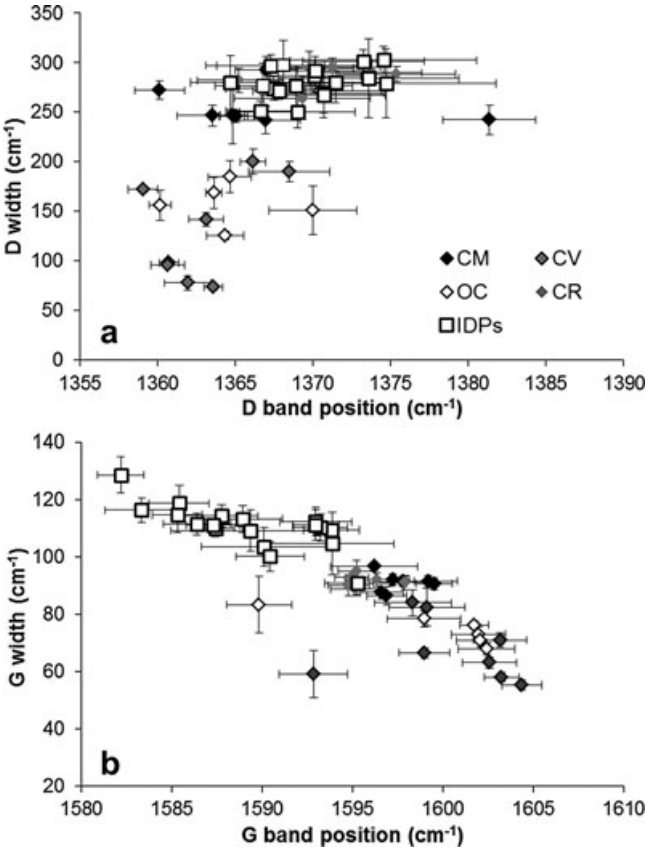

Fig. 5. Raman parameter variation diagrams for meteoritic IOM and IDPs measured by blue laser (473 nm). a) D band position against D bandwidth and b) G band position against G bandwidth. All numbers given as cm^{-1} representing the Raman shift relative to the excitation wavelength. Error bars are shown as 1σ.

The results from this study reveal an almost complete distinction between the organic matter in IDPs and that in meteoritic IOM. Only one IDP (Midford1) falls in the region defined by the meteoritic IOM based on G band parameters (Fig. 5b), albeit at the more disordered end of the IOM scale. However, another particle from the same cluster particle (Midford2) has G band parameters that indicate the presence of much more disordered carbon, revealing the extent of heterogeneity present in at least some IDPs (discussed further below). To focus on the intraparticle systematics, the full range of individual spectral data in the Raman maps used to produce the average values for each IDP (Table 2 and 3 and Figs. 2, 4, and 5) is shown for some of the samples, including Midford1, in Fig. 7 and are discussed in the Intra- and Intercluster Particle Variations section.

Intra- and Intercluster Particle Variations

The IDP samples in this study are from a selection of nine different cluster particles with each individual

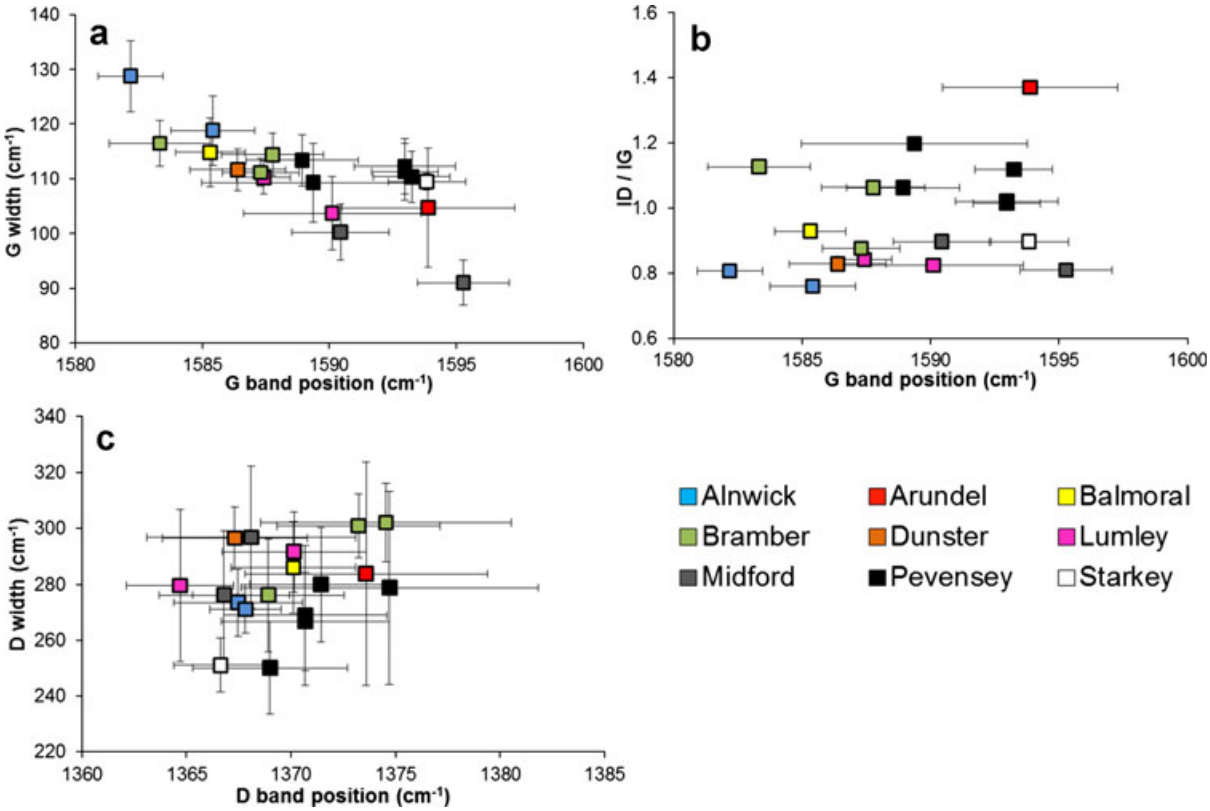

Fig. 6. a-c) Intra- and intercluster particle Raman parameter variations diagrams for IDPs measured by blue Raman laser (473 nm). All numbers given as cm^{-1} representing the Raman shift relative to the excitation wavelength. Error bars are shown as 1σ.

cluster being represented by between one and five separate cluster fragments. Figures 6a and 6c show that there is a fairly good agreement between D and G band Raman parameters from different fragments from the same IDP cluster. However, the fragments are not always within uncertainty, indicating that there is some within-cluster heterogeneity or, potentially, that they have experienced variable effects of atmospheric entry heating. Some particles display larger uncertainties reflecting greater intrafragment variability, indicating that heterogeneity is apparent at all scales in at least some particles. The negative trend between G band width and G band position, and the positive trend between I(D)/I(G) and G band position, for the IDP cluster fragments can be seen clearly in Figs. 6a and 6b, respectively. Based on the G band parameters of the IDP fragments, it is possible to define a relative scale of carbon ordering for the IDP clusters, from disordered (large G width, low G band position, and usually low I(D)/I(G)) to more ordered (small G width, high G band position, and usually high I(D)/I(G)): Alnwick < Balmoral < Dunster < Bramber < Lumley < Pevensey < Starkey2 < Arundel < Midford. Midford1 not only contains the most ordered carbon of all the IDPs measured here (it overlaps with the G band parameters for the most disordered meteoritic IOM [Fig. 5b]), but it also has a very high bulk δD (both Midford fragments have δD approximately 6000–8000‰ higher than the other samples, see the Raman Parameters Versus $\delta^{13}C$, $\delta^{15}N$, and δD Isotope Ratios for IDPs section and Fig. 8d) as reported by Starkey and Franchi (2013). This information may indicate that Midford has an origin distinct from the other particles analyzed in this study.

The degree of intraparticle heterogeneity within the meteoritic IOM and IDPs is investigated in Fig. 7. The individual data points are for the individual spectra from the Raman maps that were used to produce the average values reported in Tables 2 and 3 and Figs. 2–6. The data from some samples (e.g., Allende and MET 01017; Figs. 7a and 7b) are tightly clustered, showing a restricted range of D and G band parameters, which indicates the intrinsic reproducibility of the measurements. Most IOM and IDP samples, however, show larger intraparticle variations in G and D band parameters. The G band intraparticle trends are broadly parallel to the overall slope for the average IOM and IDP data. Allende seems to show some deviation from this trend, which may indicate higher levels of thermal metamorphism. In the other samples, the D band parameters show a limited variation in

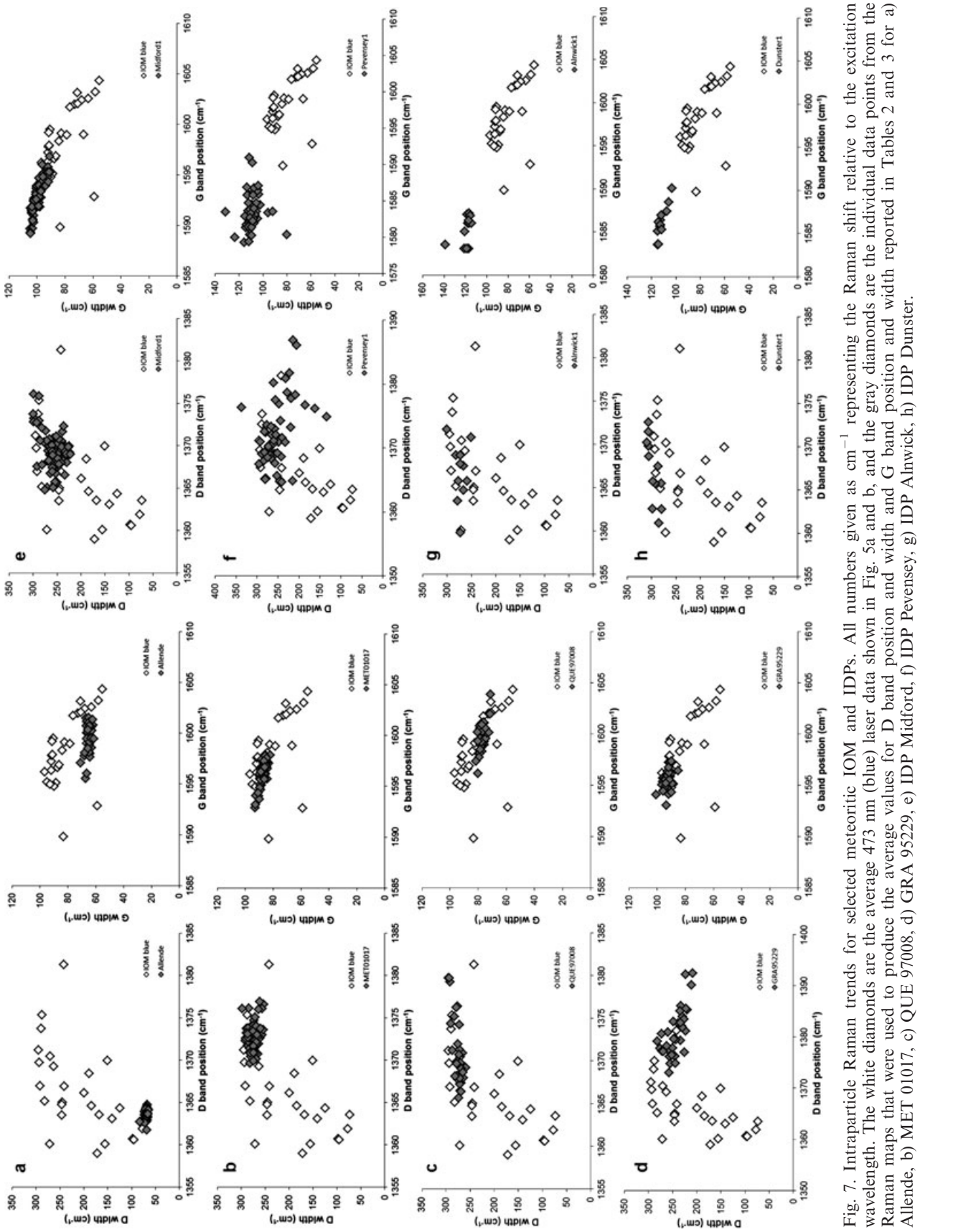

Fig. 7. Intraparticle Raman trends for selected meteoritic IOM and IDPs. All numbers given as cm^{-1} representing the Raman shift relative to the excitation wavelength. The white diamonds are the average 473 nm (blue) laser data shown in Fig. 5a and b, and the gray diamonds are the individual data points from the Raman maps that were used to produce the average values for D band position and width and G band position and width reported in Tables 2 and 3 for a) Allende, b) MET 01017, c) QUE 97008, d) GRA 95229, e) IDP Midford, f) IDP Pevensey, g) IDP Alnwick, h) IDP Dunster.

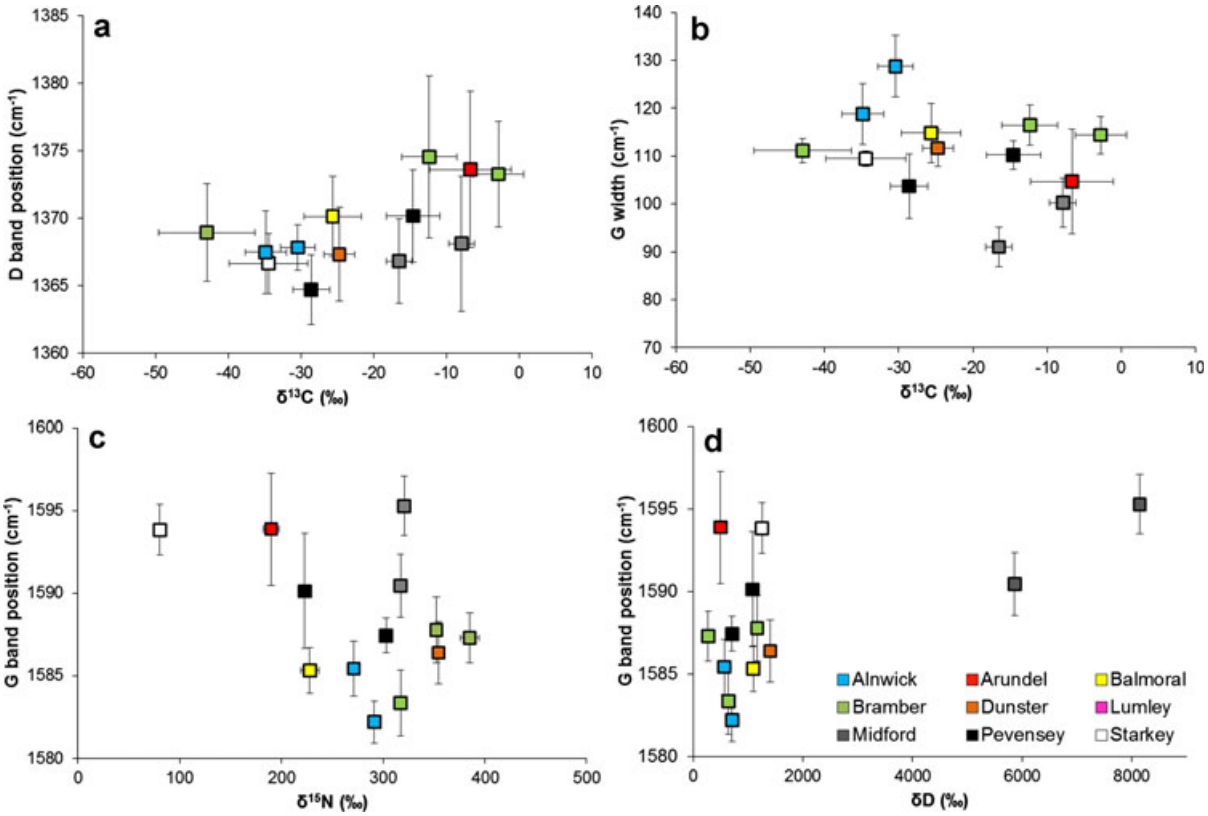

Fig. 8. Raman parameters against a–b) bulk $\delta^{13}C$, c) $\delta^{15}N$, and d) δD for IDPs (isotope data from this study [Table 3] and Starkey and Franchi [2013]). For isotope ratios, error bars are shown as 2σ.

widths, but sometimes exhibit a large range in D band position that may reflect some initial compositional heterogeneity within them. The populations of the individual spectra show some large variation in some of the IOM samples (e.g., GRA 95229 and QUE 97008; Figs. 7c and 7d), but the IDPs show the largest heterogeneity (e.g., Alnwick, Dunster, Midford, Pevensey; Figs. 7e–h). The IDP Midford, while displaying a large intraparticle variation, clusters along a tight trend in G band space, but shows more scatter in the D band. The increased scatter in the IDP intraparticle trends reflect more primitive carbon, probably reflecting multiple origins, present in these samples in comparison to the IOM and/or because of variable irradiation processing.

Raman Parameters versus $\delta^{13}C$, $\delta^{15}N$, and δD Isotope Ratios for IDPs

It has been shown previously that IDPs can display extremely anomalous H, C, and N isotopic signatures that are generally interpreted to reflect formation of the organic carriers in the cold outer regions of the protoplanetary disk or the interstellar medium (McKeegan et al. 1985; Messenger 2000; Floss et al. 2006; Aléon 2010). Comparison of the bulk isotopic values of the particles in this study (isotopic data from this study [Table 3] and Starkey and Franchi [2013]) with their Raman spectral parameters can provide further information about the provenance of the organic material and potentially the extent of parent-body processing that the IDPs have undergone. On the whole, as noted above for the Raman parameters, the bulk C and N isotopic compositions for individual fragments from any one cluster particle are fairly similar (Figs. 8a–c). One of the fragments from the Bramber cluster (Bramber4) shows a difference in $\delta^{13}C$ compared with the other two particles, highlighting the potential for small heterogeneities within the cluster, but the bulk $\delta^{15}N$ values are similar for all the Bramber fragments. Bulk δD shows more variation than bulk $\delta^{13}C$ or $\delta^{15}N$, with a 2000‰ difference in the bulk values of the two Midford particles and an 800‰ spread in the δD values for the Bramber fragments (Fig. 8d). This is consistent with previous IDP studies that have also observed large variations in bulk δD, such as Messenger (2000), Keller et al. (2004), and Floss et al. (2006).

The IDP $\delta^{13}C$ values display a positive relationship of increasing D band position (Fig. 8a; $r^2 = 0.38$,

significant at 98% level) and possibly D bandwidth ($r^2 = 0.48$, significant at 85% level), as well as a weak negative relationship with G bandwidth (Fig. 8b; $r^2 = 0.10$, significant at 70% level), but no apparent relationship with G band position ($r^2 = 0.04$). The fact that $\delta^{13}C$ becomes progressively higher as the Raman parameters tend to more ordered carbon signatures is indicative of the effects of thermal processing, as noted by Busemann et al. (2007) for meteoritic IOM. However, as discussed above, the IDPs still fall to the very primitive (disordered carbon) end of the range displayed by IOM and, therefore, any thermal processing must have been very mild, and affected a very labile component.

The IDP $\delta^{15}N$ compositions show a slightly positive relationship of D bandwidth ($r^2 = 0.18$; significant at 85% level) and a slightly negative relationship with G band position (Fig. 8c; $r^2 = 0.18$; significant at 85% level), but no relationships are apparent for D band position and G bandwidth. In general, the IDPs tend toward more normal $\delta^{15}N$ signatures as their carbon becomes progressively more ordered. However, the bulk $\delta^{15}N$ of the majority of the IDPs is high (between 200–400‰, except for IDP Starkey that has a composition of approximately 100‰), especially compared with the values for meteoritic IOM (from Alexander et al. 2007), except for Bells (CM) and the CR meteorites (and discussed in relation to their Raman parameters in Busemann et al. 2007). Busemann et al. (2007) suggested that the carrier for the high $\delta^{15}N$ found in the anomalous CM and CR chondrites IOM is very fragile because of the lower $\delta^{15}N$ in many meteorites that experienced slightly higher alteration temperatures, such as the CIs and other CMs. If correct, it is likely that the high $\delta^{15}N$ carrier in the IDPs is also fragile, but this cannot be tested readily with the IDPs in this study. IDP Starkey that falls to slightly lower $\delta^{15}N$ compared with the other IDPs also contains relatively ordered carbon and therefore is more comparable to meteoritic IOM. However, Bells and the CR IOM have comparable $\delta^{15}N$ to the IDPs, but their Raman spectra are similar to the other CMs suggesting that the picture may be more complicated.

The IDP δD values do not appear to show any strong correlations with any Raman parameters. δD against G band position is shown in Fig. 8d to indicate the extremely high δD of the Midford cluster (Starkey and Franchi 2013) in relation to the other IDPs. Figure 8d also highlights the fact that, despite the extremely elevated δD, the Raman parameters of Midford fall within the range of the other IDPs, even if Midford1 does fall at the more ordered end of the IDP spectrum and overlaps with the most disordered meteoritic IOM. Excluding the Midford fragments, there are still no clear relationships apparent in the data. This finding is in agreement with previous work on the organic material in IDPs and meteorites, where it is suggested that the D-rich carrier is aliphatic in nature (Busemann et al. 2007; Keller et al. 2004; Cody and Alexander 2005; Remusat et al. 2006). Hence, a correlation with indices of aromatic material, as evidenced by the Raman parameters, would not be expected. In addition, Dobrica et al. (2011) showed that no connection can be drawn between the Raman spectral parameters of Antarctic micrometeorites (AMM) and δD content. Alternatively, the IDPs with lower δD may have been affected by more extreme heating during atmospheric entry as it has been suggested that heating more readily affects their H isotopic compositions than that of the N isotopes (Keller et al. 2004). However, this is considered unlikely as none of the other parameters that would confirm this are in agreement. Alternatively, if aliphatic material were converted to aromatic material on heating, instead of being lost, then it could help explain the complicated relationships observed.

The high δD of Midford could be used to suggest that it is more likely to have a cometary origin than the other IDPs studied here. However, the Midford fragments do not display the fluffy porous texture usually expected for chondritic-porous (CP) IDPs that are generally considered to be the most likely particles to originate from comets (see Starkey and Franchi [2013] for FEG-SEM image of Midford). In addition, cometary particles are expected to suffer greater heating during atmospheric entry due to their inclined orbits resulting in faster entry and, as such, their H content and isotopes are more likely to be modified as the particle is heated to higher temperatures (Brownlee et al. 1995; Kehm et al. 2002). In addition, the lower G bandwidths and higher G band positions displayed by the Midford fragments (that could be used to suggest low levels of thermal metamorphism) do not seem to fit with the high δD values that would not be expected to be preserved during thermal metamorphism, even at low levels. As suggested earlier, the parent body of the Midford cluster may show some affinities to that of the ultracarbonaceous Antarctic micrometeorites (UCAMM), which are also suggested to be cometary (Dobrica et al. 2011).

DISCUSSION

Meteoritic IOM—Unraveling the Raman Parameters to Understand the Organic Matter

Estimating the degree of heating experienced by the meteoritic IOM and IDPs is an important step in understanding the history of the samples, particularly in relation to each other. However, it is not appropriate to use the temperatures inferred from calibration with

amorphous carbon annealed at different temperatures by Ferrari and Robertson (2001) for comparison with the dispersion curves of the meteoritic IOM. This is because the Ferrari and Robertson (2001) study covers a much larger range of excitation wavelengths tested on simpler carbon systems (i.e., not mixed organic material as found in meteoritic IOM). Instead, the variation in G band dispersions for the meteoritic IOM and the IDPs may indicate some relative information about the formation of their organic material. The effects of thermal metamorphism appear to induce a "V"-shaped profile in the dispersion slopes shown in Fig. 4 (i.e., in OC and CV chondrites), as described above, although it is not clear how this effect is generated. There is no systematic variation in the dispersion slope or G band position apparent with increasing metamorphic grade in the OC IOM samples. On the other hand, the reduced CV meteorites contain IOM that, while displaying the same "V"-shaped pattern as the oxidized CVs, have lower G band positions at all wavelengths. The one exception is the blue (473 nm) laser measurement of Vigarano (labeled on Fig. 4) that may reflect some level of heterogeneity. Unfortunately, no red laser measurement is available for Vigarano, making it harder to assess the pattern across the full laser range. Most of the CVs studied here experienced similar metamorphic conditions, but Leoville may have experienced shock heating to high temperatures, as evidenced by plastic deformation of its chondrules, and Allende may have been metamorphosed to temperatures in excess of 550 °C (Huss et al. 2006; Cody et al. 2008). The Allende sample displays a trend of increasing G band position with increasing excitation wavelength, which is likely to reflect the dispersion of the disorder-induced bands present in the "hybrid" G band, rather than of the G band itself, which cannot show dispersion. Busemann et al. (2007) suggested that there were distinct metamorphic sequences for the reduced and oxidized CV chondrites, although they, and Bonal et al. (2006a), did not observe any clear distinction between the two subgroups in terms of Raman peak parameters.

The comparisons made between the Raman data of this study, and the comparison of these data with the measurements in the study of Busemann et al. (2007) (Figs. 3a and 3b) provide some clues as to the practicality of Raman as a technique for understanding the organic material in chondrites, and particularly the level of thermal metamorphism they may have experienced. The correlation of the Raman parameters for the type 3 chondrite IOM data on an individual meteorite basis between studies, and between different wavelengths in this study, and the lack of correlation of the type 2 chondrites, reveal the potential for heterogeneity at the individual particle level in the type 2 chondrite IOM. In each of these studies, although the same IOM residue was measured for each chondrite, the exact particle that was measured did differ. A conclusion that can be drawn from Fig. 3 is that if the lack of correlation in the type 2 chondrites is indeed down to heterogeneity of the organic material present at the individual IOM dispersed particle level, then it can be assumed that the thermal metamorphism process that occurred to produce the type 3 chondrites also acted to drive the structure of originally heterogeneous IOM, such as found in type 2 chondrites, toward a common endmember composition (i.e., a more homogeneous IOM structure). The larger uncertainties associated with the mean values for G band position for the individual type 2 chondrite data are consistent with greater heterogeneity for these IOM samples compared with IOM from type 3 chondrites. In addition, the individual slopes for the dispersion trends (Fig. 4) for the type 2 chondrites are also more likely to show cross-cutting patterns in relation to each other (i.e., the type 2s are less conformable) than those of the type 3 chondrites. Interestingly, in the CM and CR groups, the total range displayed by the mean values is less than a typical 1σ of the mean from any one meteorite, whereas the type 3 chondrites show a much greater spread than is observed within any one meteorite. These findings suggest that it would be difficult to use Raman as a technique to look for differences between chondrites of lower petrographic type without sampling very large areas, but that Raman may be of considerable use in the characterization of IOM at a local ($\approx$micron) scale.

The narrow range in G band position displayed by the CR and CM meteorites, combined with the heterogeneous nature of these samples, means it is unsurprising that there is little evidence for any systematic variation in the Raman peak parameters in relation to changes in the extent of aqueous alteration experienced by these samples. This finding is in agreement with Bonal et al. (2013), who report that the Raman characteristics of the CRs do not relate to their level of aqueous alteration. This leads us to conclude that the degree of aqueous alteration has little effect on the Raman signature of the IOM. This, in turn, suggests that aqueous alteration acts primarily on the less Raman-active functional groups and cross-linking structures, while the more Raman active core aromatic structures within the IOM are largely unaffected. Despite the heterogeneity within each sample, there is a consistent marked G band dispersion in the CM IOM, while there is essentially no dispersion for the CR chondrite samples (Fig. 4). There were, undoubtedly, some largely subtle differences in the nature of the alteration on the CM and CR parent bodies. However,

as indicated by the lack of Raman variation between CMs and CRs in this study, these differences would be unlikely to have had a major impact on the Raman active core structure. Therefore, the difference in dispersion behavior between the CMs and CRs may point to differences in the original accreted material.

IDPs—Raman Parameters of Organic Matter in IDPs and Comparison with Meteoritic IOM

With one exception (Midford; see below), the IDPs in this study display lower G band positions and larger G bandwidths than any of the IOM samples (Fig. 5b), indicating that the IDPs contain more disordered organic carbon than the chondritic IOM. Previous work by Busemann et al. (2009) revealed that approximately 30% of the IDPs they studied had G band parameters overlapping with those of the CR IOM. Low G band positions have been documented in the literature for other IDPs and interpreted as being due to ion irradiation in icy mantles in the protoplanetary disk or interstellar medium, or due to irradiation in interplanetary space as the particles spiraled toward the Earth (Ferini et al. 2004; Nittler et al. 2006), a signature that is destroyed by even low-temperature thermal processing (Busemann et al. 2007). The study by Ferini et al. (2004) compared the Raman spectra of a set of IDPs with those of synthetic irradiated icy mixtures to investigate whether their amorphous carbon could result from the ion irradiation of volatile materials in the parent bodies of the IDPs. However, the results were inconclusive, suggesting that more work is required to understand the irradiation of cometary ices. Nevertheless, Busemann et al. (2009) showed that the same feature, of extremely low G band position, can be found in some primitive meteorites, which they also suggested indicated similar formation processes as the IDPs, i.e., preaccretionary ion irradiation of icy mixtures in the protoplanetary disk of the interstellar medium.

Although the G band parameters of the IDPs are distinct from the IOM samples, it is interesting to note that all the meteoritic IOM samples (OC, CV, CM, and CR) and IDP samples appear to define a single common trend (Fig. 5b) that could be used to suggest a shared evolutionary path. Previous work by Busemann et al. (2009) revealed a similar common evolution for IDPs extending from the more carbon-rich carbonaceous chondrites (CM, CR, CI meteorites). However, the study by Busemann et al. (2007) showed that IOM from type 3 meteorites had G band parameters that appear to define a distinct evolutionary trend, with lower G band width at comparable G band position. The samples used in our study were aliquots of the same samples analyzed by Busemann et al. (2007). Peak fitting of test spectra that are characteristic of type 2 and type 3 carbonaceous chondrites revealed no systematic differences between the procedures used by Busemann et al. (2007) and those used in this study, that are essentially identical to the methods employed in the study of Rotundi et al. (2008). However, in contrast to the results of Busemann et al. (2007), the distinction between type 1–2 and type 3 IOM in our results is less apparent (Fig. 5). This result is consistent with both the blue (473 nm) and green (514 nm) lasers and, therefore, it is unlikely that the difference between our study and that of Busemann et al. (2007) is related to excitation laser wavelength. Further interlaboratory (or interinstrument) comparisons are required to understand these differences, but the differences highlight the difficulties of comparing results that were not acquired under identical conditions. The results from this study are more consistent with a common origin for most of the organic material in the main chondrite groups and IDPs, with the IDPs simply representing the more primary, disordered carbonaceous material. It should be noted, however, that differences do exist in some of the organic components in IDPs and meteoritic IOM. It is possible that discrete N-rich areas present in IDPs may reflect the presence of an additional accreted component to the IDP source, with the bulk of the organic matter in meteorites and IDPs still sharing a common origin. Alternatively, if the organic matter in IDPs represents the precursor material for meteoritic IOM then additional processes, such as aqueous alteration or thermal processing, could account for the loss of N-rich material in the meteoritic IOM.

The disordered carbon G band parameters of the IDPs support the argument that they did not experience sustained thermal metamorphism. The effects of atmospheric entry heating on IDPs are not well understood, particularly in terms of the organics. IDPs may be flashheated to over 500 °C as they enter the Earth's stratosphere (Love and Brownlee 1991), as evidenced by the formation of magnetite rims on some IDPs (Thomas et al. 1992), and which may also cause some chemical modification through loss of H, and volatile species (Kehm et al. 2002). The absence of increased ordering of the carbon, however, may be controlled by the slow kinetics of the heating during atmospheric entry such that structures controlling the Raman parameters are largely insensitive to the heating effects. The Raman parameters derived from the organic material in the IDPs of our study indicate that they did not experience, or are insensitive to the effects of, significant heating. More work will be required to fully understand the role of atmospheric entry heating on the organic material in IDPs.

The high δD values of organic matter in primitive extraterrestrial materials are often taken to indicate an

origin in the outer disk or interstellar medium, and that preservation of this high δD also indicates that the sample underwent very little, or no, interaction with isotopically light water or H_2 in the protoplanetary disk or on a parent body. The high δD and the disordered Raman peak parameters of Midford, therefore, may reflect the signature of a primary unprocessed D′ component in the early solar system. It is noted that the aromatic component in Midford is relatively ordered for an IDP, but at the very disordered end of the range displayed by meteoritic IOM. Irradiation of IOM-like material has been proposed as a mechanism to generate the highly disordered organic material observed in IDPs (e.g., Ferini et al. 2004; Nittler et al. 2006; Busemann et al. 2007). If this occurred in the protoplanetary disk, the D-rich organic matter may also have had the opportunity to exchange with abundant D-poor water (D-poor in relation to Midford, but still a δD of possibly 500-1000‰) present throughout most of the disk. Exposure of dust, freed from its parent asteroid, to the disordering effects of radiation in interplanetary space seems like an unlikely mechanism to account for the very disordered nature of these IDPs. This is because IDPs from the Grigg-Skjellerup collection (GSC) analyzed by Busemann et al. (2009) had, in general, more disordered carbon than those IDPs from the general background flux, despite the relatively short transfer times of particles released from the Grigg-Skjellerup comet to Earth, suggesting that recent exposure is not the origin of the disordering of carbon in those IDPs. However, the provenance of any individual IDP, even in the GSC, is unknown and the limited number of particles that have been analyzed makes definitive conclusions difficult. Indeed, Davidson et al. (2012) concluded that, although there may be a difference in Raman peak parameters between the GSC particles and those from the background flux of IDPs, there are no discernible differences in their C, N, and H isotope ratios (although again this was based on a limited number of particles). Therefore, the variation in Raman parameters for IDP OM appears to reflect primary processes from the protoplanetary disk (or earlier). This original material may have had a structure comparable to the OM in IDPs, which has the highest G band positions, as ion irradiation processes in the early disk may then have extended the diversity of molecular structure to even lower G band positions. The meteoritic IOM, on the other hand, accreted the same starting material (variably processed primary components from the protoplanetary disk) that may then have experienced differing levels of secondary processing on their asteroidal parent bodies that had the effect of creating more ordering of the organic component with increasing alteration. The principal controlling parameter would have been temperature, and generally in the presence of D-poor water that would drive down the δD of the organics through reaction and exchange.

The degree of structural order of carbon in the IDPs could reflect differences in the formation of the organics present, with increased disordering resulting from irradiation or increased ordering from thermal processing (in the protoplanetary disk, parent body, or during atmospheric entry). It seems likely that the OM in all IDPs shares a genetic link as it falls on a common linear trend in the plot of G band position versus G bandwidth (Fig. 5b). Dobrica et al. (2011) showed that the fine-grained Antarctic micrometeorites (AMMs) and ultracarbonaceous AMMs (UCAMMs) analyzed by Raman did not experience significant heating during atmospheric entry, or long duration heating on the parent body, as they retained a high degree of disorder similar to the IDPs analyzed here. Interestingly, UCAMMs can also show elevated δD (Duprat et al. 2010), indicating a potential link between the UCAMM and IDP parent bodies, or at least that of the Midford cluster. However, UCAMM also have similar δD and H/C to some mildly metamorphosed OCs, indicating that δD alone may not best be used to infer a genetic relationship. Therefore, whether the parent body for IDPs is best represented by a primitive asteroid or a comet is still open to question.

SUMMARY AND IMPLICATIONS

This study has used Raman measurements taken with multiple excitation wavelengths to further characterize the variations observed in the Raman peak parameters of amorphous carbon in meteoritic IOM from a number of different meteorite groups, characterizing different parent-body processes, and to explore the relationship between meteoritic IOM and organic matter in IDPs. The variations in Raman D and G bands for meteoritic IOM observed from a single excitation wavelength (e.g., 473 nm blue) are generally consistent with previous studies employing longer wavelengths. The common or related Raman parameters for the meteoritic IOM strongly argue for a common origin for the IOM in different meteorite groups that are then affected by aqueous alteration and thermal metamorphism in a broadly similar manner.

The Raman peak parameters from any sample change as a function of the excitation laser wavelength (dispersion). Crucially, the dispersion varies as a function of the degree of ordering and the D band position dispersion is approximately linear with excitation wavelength. However, neither D nor G bandwidths vary with excitation wavelength. There is an increase in dispersion between green and blue lasers over that between red and green lasers and this is

greatest in CVs > OCs > CMs > CRs. The multiwavelength comparison of Raman parameters between IDPs and IOM shows that the D band dispersion of the IDPs is broadly linear (like the CMs and CRs) and that the slope of this dispersion with excitation wavelength is most similar to the CRs. The G band dispersion of the IDPs is fairly weak (G band position decreasing with increasing wavelength; mostly like CRs) and the G band dispersion is generally greater between green and blue lasers than that between red and green lasers. The single-wavelength study of IOM and IDPs shows that the D band positions and widths in the IDPs are essentially indistinguishable from those in CMs and CRs. The G band position and width of the IDPs fall on an extension (to more disordered carbon) of the trend of G bandwidth versus G band position defined by IOM, with virtually no overlap.

These data demonstrate that dispersion varies as a function of the nature of the organic material present. This is evidenced most clearly by the lack of conformity in type 2 chondrite IOM Raman measurements carried out at different excitation wavelengths in comparison to the good correlation for type 3 chondrite IOM. It is, therefore, essentially impossible to apply a systematic correction that would permit direct comparison of results obtained with different excitation wavelengths.

The IDPs of this study, in agreement with the results of previous IDP Raman studies (Wopenka 1988; Quirico et al. 2005; Bonal et al. 2006b; Busemann et al. 2009), display very disordered carbon, which, in most cases, corresponds with high $\delta^{15}N$, low $\delta^{13}C$ and, in some cases, anomalously high δD. These characteristics all suggest that the IDPs preserve pristine organic matter. The origin of the high δD and $\delta^{15}N$ signatures in IDPs is currently unknown. Formation locations that have been suggested to account for such enrichments are the cold outer reaches of the protoplanetary disk (Aléon 2010; Remusat et al. 2006, 2009; Duprat et al. 2010) or the interstellar medium. Either way, a requirement is that the enrichments need to be distributed homogenously throughout the comet-forming region, as such signatures are found in a wide range of IDPs and meteorites. It has been speculated that the source for the organic matter in IDPs is related to the OCs as they show some similarities in terms of mineralogy (Alexander et al. 1989), but the results from this study do not support such a conclusion. In addition, Dobrica et al. (2011) show that Raman spectra of AMM in the 20–500 μm size range show more similarities to CCs as opposed to OCs, whereas larger AMM particles (>500 μm) have been shown to have affinities to OCs (Rochette et al. 2008). The fine-grained texture of IDPs is perhaps more similar to that of the ungrouped CO-CM meteorite Acfer094 (Greshake 1997). However, the very disordered nature of the carbon in IDPs, as demonstrated here and in other studies, suggests that the meteorite groups are unlikely to represent the source for IDPs.

The variability in Raman parameters measured between different IDP cluster particles could reflect differences in the composition of the material originally accreted to parent bodies, to secondary processing on the parent body, or to a mixture of processes occurring before and after accretion. Either way, the variations in the IDPs are quite large compared with the variability observed within individual meteorite groups. The conformity of some of the Raman parameters for meteoritic IOM and IDPs in this study is in agreement with some previous studies, suggesting that meteorites and IDPs may have accreted similar precursor organic material. The main difference being that the organic matter in the meteorite parent bodies underwent subsequent parent-body processing, whereas the parent bodies of the IDPs appear to have undergone very little, or no, processing such that they preserved very disordered Raman parameters.

Acknowledgments—The authors would like to thank Wayne Twigger and Simon FitzGerald at Horiba Ltd. (UK) for useful discussion regarding red laser analyses and also for the use of their Raman system for tests. We would also like to thank E. Quirico and B. Wopenka for detailed and helpful reviews that significantly helped to improve the manuscript and D. Brownlee for handling the editing. The Meteorite Working Group is thanked for samples. The authors acknowledge funding from Science and Technology Facilities Council (STFC) rolling grant (ST/I001964/1) to NAS/IAF and UKCAN for NanoSIMS access.

Editorial Handling—Dr. Donald Brownlee

REFERENCES

Abreu N. M. and Brearley A. J. 2010. Early solar system processes recorded in the matrices of two highly pristine CR3 carbonaceous chondrites, MET 00426 and QUE 99177. *Geochimica et Cosmochimica Acta* 74:1146–1171.

Aléon J. 2010. Multiple origins of nitrogen isotopic anomalies in meteorites and comets. *The Astrophysical Journal* 722:1342–1351.

Aléon J., Engrand C., Robert F., and Chaussidon M. 2001. Clues to the origin of interplanetary dust particles from the isotopic study of their hydrogen-bearing phases. *Geochimica et Cosmochimica Acta* 65:4399–4412.

Alexander C. M. O'D., Barber D. J., and Hutchison R. 1989. The microstructure of Semarkona and Bishunpur. *Geochimica et Cosmochimica Acta* 53:3045–3057.

Alexander C. M. O'D., Russell S. S., Arden J. W., Ash R. D., Grady M. M., and Pillinger C. T. 1998. The origin of chondritic macromolecular organic matter: A carbon and

nitrogen isotope study. *Meteoritics & Planetary Science* 33:603–622.

Alexander C. M. O'D., Fogel M., Yabuta H., and Cody G. D. 2007. The origin and evolution of chondrites recorded in the elemental and isotopic compositions of their macromolecular organic matter. *Geochimica et Cosmochimica Acta* 71:4380–4403.

Alexander C. M. O'D., Newsome S. D., Fogel M. L., Nittler L. R., Busemann H., and Cody G. D. 2010. Deuterium enrichments in chondritic macromolecular material—Implications for the origin and evolution of organics, water and asteroids. *Geochimica et Cosmochimica Acta* 74:4417–4437.

Bonal L., Quirico E., Bourot-Denise M., and Montagnac G. 2006a. Determination of the petrologic type CV3 chondrites by Raman spectroscopy of included organic matter. *Geochimica et Cosmochimica Acta* 70:1849–1863.

Bonal L., Quirico E., Montagnac G., and Reynard B. 2006b. Interplanetary dust particles: Organic matter studied by Raman spectroscopy and laser induced fluorescence (abstract #2271). 37th Lunar and Planetary Science Conference. CD-ROM.

Bonal L., Bourot-Denise M., and Quirico E. 2007. Organic matter and metamorphic history of CO chondrites. *Geochimica et Cosmochimica Acta* 71:1605–1623.

Bonal L., Alexander C. M. O'D, Huss G. R., Nagashima K., Quirico E., and Beck P. 2013. Hydrogen isotopic composition of the water in CR chondrites. *Geochimica et Cosmochimica Acta* 106:111–133.

Brownlee D. E., Joswiak D. J., Schlutter D. J., and Bradley J. P. 1995. Identification of individual cometary IDPs by thermally stepped He release (abstract). 26th Lunar and Planetary Science Conference. p. 183.

Busemann H., Young A. F., Alexander C. M. O'D., Hoppe P., Mukhopadhyay S., and Nittler L. R. 2006. Interstellar chemistry recorded in organic matter from primitive meteorites. *Science* 312:727–730.

Busemann H., Alexander C. M. O'D., and Nittler L. R. 2007. Characterization of insoluble organic matter in primitive meteorites by microRaman spectroscopy. *Meteoritics & Planetary Science* 42:1387–1416.

Busemann H., Nguyen A. N., Cody G. D., Hoppe P., Kilcoyne A. L. D., Stroud R. M., Zega T. J., and Nittler L. R. 2009. Ultra-primitive interplanetary dust particles from the comet 26P/Grigg-Skjellerup dust stream collection. *Earth and Planetary Science Letters* 288:44–57.

Cody G. D. and Alexander C. M. O'D. 2005. NMR studies of chemical and structural variation of insoluble organic matter from different carbonaceous chondrite groups. *Geochimica et Cosmochimica Acta* 69:1085–1097.

Cody G. D., Alexander C. M. O'D., and Tera F. 2002. Solid-state (^{1}H and ^{13}C) nuclear magnetic resonance spectroscopy of insoluble organic residue in the Murchison meteorite: A self-consistent quantitative analysis. *Geochimica et Cosmochimica Acta* 66:1851–1865.

Cody G. D., Alexander C. M. O'D., Yabuta H., Kilcoyne A. L. D., Araki T., Ade H., Dera P., Fogel M., Militzer B., and Mysen B. O. 2008. Organic thermometry for chondritic parent bodies. *Earth and Planetary Science Letters* 272:446–455.

Cody G. D., Heying E., Alexander C. M. O'D., Nittler L. R., David Kilcoyne A. L., Sandford S. A., and Stroud R. M. 2011. Establishing a molecular relationship between chondritic and cometary organic solids. *Proceedings of the National Academy of Sciences* 108:19171–19176.

Davidson J., Busemann H., and Franchi I. A. 2012. A NanoSIMS and Raman spectroscopic comparison of interplanetary dust particles from comet Grigg-Skjellerup and non-Grigg Skjellerup collections. *Meteoritics & Planetary Science* 4:1748–1771.

Dobrica E., Engrand C., Quirico E., Montagnac G., and Duprat J. 2011. Raman characterization of carbonaceous matter in CONCORDIA Antarctic micrometeorites. *Meteoritics & Planetary Science* 46:1363–1375.

Duprat J., Dobrica E., Engrand C., Aléon J., Marocchi Y., Moustefaoui S., Meibom A., Leroux H., Rouzaud H.-N., Gounelle M., and Rovert F. 2010. Extreme deuterium excesses in ultracarbonaceous micrometeorites from Central Antarctic snow. *Science* 328:742–745.

Ferini G., Baratta G. A., and Palumbo M. E. 2004. A Raman study of ion irradiated icy mixtures. *Astronomy and Astrophysics* 414:757–766.

Ferrari A. C. and Robertson J. 2000. Interpretation of Raman spectra of disordered and amorphous carbon. *Physical Review B* 61:14095–14107.

Ferrari A. C. and Robertson J. 2001. Resonant Raman spectroscopy of disordered, amorphous, and diamondlike carbon. *Physical Review B* 64:075414.

Floss C., Stadermann F. J., Bradley J. P., Dai Z. R., Bajt S., Graham G., and Lea A. S. 2006. Identification of isotopically primitive interplanetary dust particles: A NanoSIMS isotopic imaging study. *Geochimica et Cosmochimica Acta* 70:2371–2399.

Fraundorf P., Patel R. I., Swan P. R., Walker M., Adar F., and Freeman J. J. 1982. Vibrational microspectroscopy of interplanetary dust in the laboratory. In *Microbeam analysis*, edited by Heinrich K. F. J. San Francisco, California: San Francisco Press. pp. 188–190.

Gilmour I. 2003. Structural and isotopic analysis of organic matter in carbonaceous chondrites. In *Meteorites, comets, and planets*, edited by Davis A. M. Treatise on Geochemistry, vol. 1. Amsterdam: Elsevier. pp. 269–290.

Greshake A. 1997. The primitive matrix components of the unique carbonaceous chondrite Acfer 094: A TEM study. *Geochimica et Cosmochimica Acta* 61:437–452.

Hayatsu R., Matsuoka S., Scott R. G., Studier M. H., and Anders E. 1977. Origin of organic matter in the early solar system-VII. The organic polymer in carbonaceous chondrites. *Geochimica et Cosmochimica Acta* 41:1325–1339.

Huss G., Rubin A. E., and Grossman J. N. 2006. Thermal metamorphism in chondrites. In *Meteorites and the early solar system II*, edited by Lauretta D. and McSween H. Y. Jr. Tucson, Arizona: Arizona University Press. pp. 567–586.

Kehm K., Flynn G. J., Sutton S. R., and Hohenberg C. M. 2002. Combined noble gas and trace element measurements of individual stratospheric interplanetary dust particles. *Meteoritics & Planetary Science* 37:1323–1335.

Keller L. P., Messenger S., Flynn G. J., Clemett S., Wirick S., and Jacobsen C. 2004. The nature of molecular cloud material in interplanetary dust. *Geochimica et Cosmochimica Acta* 68:2577–2589.

Love S. G., and Brownlee D. E. 1991. Heating and thermal transformation of micrometeoroids entering Earth's atmosphere. *Icarus* 89:26–43.

Matthews M. J., Pimenta M. A., Dresselhaus G., and Endo M. 1999. Origin of dispersive effects of the Raman D band in carbon materials. *Physical Review B* 59(10):6585–6588.

McKeegan K. D., Walker R. M., and Zinner E. 1985. Ion microprobe measurements of individual interplanetary dust particles. *Geochimica et Cosmochimica Acta* 49:1971–1987.

Messenger S. 2000. Identification of molecular-cloud material in interplanetary dust particles. *Nature* 404:968–971.

Messenger S., Clemett S. J., Keller L. P., Thomas K. L., Chillier X. D. F., and Zare R. N. 1995. Chemical and mineralogical studies of an extremely deuterium-rich IDP. *Meteoritics* 30:546–547.

Nittler L. R., Busemann H., and Hoppe P. 2006. Isotopic and micro-Raman investigation of interplanetary dust particles collected during 2003 Earth passage through comet Grigg-Skjellerup dust stream (abstract #2301). 37th Lunar and Planetary Science Conference. CD-ROM.

Quirico E., Raynal P.-I., and Bourot-Denise M. 2003. Metamorphic grade of organic matter in six unequilibrated ordinary chondrites. *Meteoritics & Planetary Science* 38:795–811.

Quirico E., Borg J., Raynal P.-I., Montagnac G., and D'Hendecourt L. 2005. A micro-Raman survey of 10 IDPs and 6 carbonaceous chondrites. *Planetary and Space Science* 53:1443–1448.

Remusat L., Derenne S., and Robert F. 2005. New insight on aliphatic linkages in the macromolecular organic fraction of Orgueil and Murchison meteorites through ruthenium tetroxide oxidation. *Geochimica et Cosmochimica Acta* 69:4377–4386.

Remusat L., Palhol F., Robert F., Derenne S., and France-Lanord C. 2006. Enrichment of deuterium in insoluble organic matter from primitive meteorites: A solar system origin? *Earth and Planetary Science Letters* 243:15–25.

Remusat L., Robert F., Meibom A., Mostefaoui S., Delpox O., Binet L., Gourier D., and Derenne S. 2009. Proto-planetary disk chemistry recorded by D-rich organic radicals in carbonaceous chondrites. *The Astrophysical Journal* 698:2087–2092.

Remusat L., Guan Y., Wang Y., and Eiler J. M. 2010. Accretion and preservation of D-rich organic particles in carbonaceous chondrites: Evidence for important transport in the early solar system nebula. *The Astrophysical Journal* 713:1048.

Robert F., Derenne S., Thomen A., Anquetil C., and Hassouni K. 2011. Deuterium exchange rate between D3 + and organic CH bonds: Implication for D enrichment in meteoritic IOM. *Geochimica et Cosmochimica Acta* 75:7522–7532.

Rochette P., Folco L., Suavet C., van Ginneken M., Gattacceca J., Perchiazzi N., Braucher R., and Harvey R. 2008. Micrometeorites from the Transantarctic Mountains. *Proceedings of the National Academy of Sciences* 105:18206–18211.

Rotundi A., Baratta G. A., Borg J., Brucato J. R., Busemann H., Colangeli L., D'Hendecourt L. D., Djouadi Z., Ferrini G., Franchi I. A., Fries M., Palumbo M. E., Sandford S. A., Steele A., and Wopenka B. 2008. Combined micro-Raman, micro-infrared, and field emission scanning electron microscope analyses of comet 81P/Wild 2 particles collected by Stardust. *Meteoritics & Planetary Science* 43:367–397.

Rubin A. E., Trigo-Rodriguez J. M., Huber H., and Wasson J. T. 2007. Progressive aqueous alteration of CM carbonaceous chondrites. *Geochimica et Cosmochimica Acta* 71:2361–2382.

Sandford S. A., Aléon J., Alexander C. M. O'D., Araki T., Bajt S., Baratta G. A., Borg J., Bradley J. P., Brownlee D. E., Brucato J. R., Burchell M. J., Busemann H., Butterworth A., Clemett S. J., Cody G., Colangeli L., Cooper G., D′ Hendecourt L., Djouadi Z., Dworkin J. P., Ferrini G., Fleckenstein H., Flynn G., Fries M., Gilles M. K., Glavin D. P., Gounelle M., Grossemy F., Jacobsen C., Kilcoyne D., Leitner J., Matrajt G., Meibom A., Mennella V., Mostefaoui S., Nittler L. R., Palumbo M. E., Robert F., Rotundi A., Snead C. J., Spencer M. K., Stadermann F. J., Steele A., Stephan T., Tsou P., Tyliszczak T., Westphal A. J., Wirick S., Wopenka B., Yabuta H., Zare R. N., and Zolensky M. E. 2006. Organics captured from comet Wild-2 by the Stardust spacecraft. *Science* 314:1720–1724.

Schramm L. S., Brownlee D. E., and Wheelock M. M. 1989. Major element composition of stratospheric micrometeorites. *Meteoritics* 24:99–112.

Sephton M. A., Love G. D., Meredith W., Snape C. E., Sun C.-G., and Watson J. S. 2005. Hydropyrolysis: A new technique for the analysis of macromolecular material in meteorites. *Planetary and Space Sciences* 53:1280–1286.

Starkey N. A. and Franchi I. A. 2013. Insight into the silicate and organic reservoirs of the comet forming region. *Geochimica et Cosmochimica Acta* 105:73–91.

Thomas K. L., Keller L. P., Flynn G. J., Sutton S. R., Takatori K., and McKay D. S. 1992. Bulk compositions, mineralogy, and trace element abundances of six interplanetary dust particles (abstract #1427). 23rd Lunar and Planetary Science Conference. p. 1427.

Tuinstra F. and Koenig J. L. 1970. Raman spectrum of graphite. *The Journal of Chemical Physics* 53:1126–1130.

Vidano R. P., Fishbach D. B., Willis L. J., and Loehr T. M. 1981. Observation of Raman band shifting with excitation wavelength for carbons and graphites. *Solid State Communications* 39:341–344.

Wang Y., Alsmeyer D. C., and McCreery R. L. 1990. Raman spectroscopy of carbon materials: Structural basis of observed spectra. *Chemical Materials* 2:557–563.

Wopenka B. 1988. Raman observations on individual interplanetary dust particles. *Earth and Planetary Science Letters* 88:221–231.

Yang J. and Epstein S. 1983. Interstellar organic matter in meteorites. *Geochimica et Cosmochimica Acta* 47:2199–2216.